TÉCNICO LISBOA

Dimensioning of a traction motor for the Formula Student Técnico (FST) using a Vanadium-Cobalt-Iron alloy

António da Conceição Cardoso

Thesis to obtain the Master of Science Degree in

Electrical and Computer Engineering

Supervisor: Prof. Dr. João Filipe Pereira Fernandes

Examination Committee

Chairperson: Prof.ª Dra. Célia Maria Santos Cardoso de Jesus
Supervisor: Prof. Dr. João Filipe Pereira Fernandes
Member of the Committee: Prof. Dr. Vitor Manuel de Oliveira Maló Machado

October 2020

Declaration

I declare that this document is an original work of my own authorship and that it fulfills all the requirements of the Code of Conduct and Good Practices of the Universidade de Lisboa.

Acknowledgments

I would first like to thank my thesis advisor Prof. Dr. João Filipe Pereira Fernandes whose expertise was invaluable in formulating the research methodology and consistently allowed this paper to be my own work, but steered me in the right direction whenever he thought I needed it.

I would also like to acknowledge Pedro Bhagubai for his patient support and valuable guidance throughout my dissertation.

I would like to show gratitude to the FST team for making this topic possible.

A big thank you to my parents my sister and all my family who provided me with their wise counsel and unconditional support in every single achievement of my life.

I am also grateful to my course and LME colleagues for the support along this long run.

Finally, I would like to thank all my friends and teammates that helped me be the person I am today.

Resumo

Veículos elétricos e híbridos têm sofrido um recente crescimento, devido ao desenvolvimento de novas tecnologias relacionadas à maximização do rendimento e da sua potência específica. Entre estas, a aplicação de técnicas de otimização e o uso de novos materiais eletromagnéticos são procedimentos que têm sido exploradas recentemente. Neste trabalho, uma máquina síncrona de ímanes permanentes é otimizada para ser usada como motor de um carro elétrico da competição Formula Student, requerendo alto desempenho com um alto rácio de potência/volume.

Dois diferentes materiais magnéticos foram testados para serem usados no núcleo do motor: o típico Ferro-Silício (FeSi) e Vanádio-Cobalto-Ferro (VCoFe). Este projeto pretende definir em que condições a utilização da liga de VCoFe, caracterizada pelo seu alto ponto de saturação 2.2-2.4 T, pode ser vantajosa em comparação com a liga de FeSi.

Uma otimização de multiobjetivo foi desenvolvida para identificar os melhores parâmetros e o desenho da máquina, com especial atenção ao seu rendimento e potência específica, cumprindo sempre os constrangimentos. Esta otimização foi executada com o algoritmo NSGA-II acoplado a um modelo analítico e um método de elementos finitos, providenciando resultados suficientemente precisos com um tempo de computação fazível.

Resultados demonstram que o uso do VCoFe como material do núcleo providencia mais benefícios na potência específica quando comparado com o FeSi. Superando este num aumento estimado de 3% de rendimento, para o mesmo valor de binário, e um aumento de até 70% de binário para o mesmo rendimento. Para o veículo da FST, com um binário de 20 Nm, observou-se um aumento de 1.7% de rendimento e uma redução de 11% do volume do motor.

Palavras-Chave: Ferro-Silício, Máquina síncrona de ímanes permanentes, Método de elementos finitos, Modelo electromagnético, Otimização de multiobjetivo.

Abstract

Hybrid and fully electric vehicles have pursued a recent growth and, along with this, new electric machines technologies are being developed focusing on increasing efficiency and specific power through the application of optimisation techniques and new materials. In this work, a high specific-power spoke-type Interior Permanent Magnet Synchronous Machine (IPMSM) for the competition's FST electric car has been optimised, demanding high-performance requirements with a large ratio of power/volume.

Two different magnetic materials were tested for the motor's magnetic core: the typical Silicon-Iron alloy (FeSi) and a Vanadium-Cobalt-Iron alloy (VCoFe) alloy. This project attempts to define in which conditions the VCoFe alloy, holding a remarkable high saturation point of 2.2-2.4 T, provides advantages in this application, over the FeSi.

Multi-objective optimisation was developed to identify the best parameters and machine designs, using VCoFe and FeSi, regarding specific power and efficiency, while fulfilling the relevant applicable constraints. The optimisation was done using the Non-dominated Sorting Genetic Algorithm II (NSGA-II) algorithm coupled with a hybrid analytical/finite element method to provide sufficiently accurate electromagnetic and thermal results within a feasible time.

Results demonstrate VCoFe as a beneficial core material, providing higher specific power than FeSi. Outperforming FeSi in an estimated increase of up to 3% in efficiency for the same torque, or up to 70% torque increase for the same efficiency level. For the FST competition car, with a required 20 Nm of nominal torque, there is an efficiency increase of 1.7% and a reduction of 11% in core volume for the motor.

Keywords: Electric vehicle, Electromagnetic modelling, Finite element method, Multi-objective optimisation, Permanent magnet synchronous machine, Silicon-Iron, Vanadium-Cobalt-Iron.

Contents

List of Tables

List of Figures

Nomenclature

Greek symbols

η	Efficiency [%]
μ_r	Relative magnet permeability
ω_e	Electrical speed [s^{-1}]
ω_m	Mechanical speed [s^{-1}]
ω_{me}	Field mechanical speed [s^{-1}]
Ψ_d,Ψ_q	Direct and quadrature linked flux [Wb]
Ψ_{PM}	Permanent magnet linked flux [Wb]
$\Psi_{PM,d}$	Direct permanent magnet linked flux [Wb]
ρ_{cu}	Copper resistivity [Ω/m]
ρ_{PM}	Permanent magnet resistivity [Ω/m]
σ_{air}	Electric conductivity of air [S/m]
θ_{me}	Mechanical angle position [$^\circ$]
θ_r	Rotor mechanical angle position [$^\circ$]
θ_s	Stator mechanical angle position [$^\circ$]

Roman symbols

abc	Stationary coordinate system
A_{slot}	Coil slot area [m^2]
B	Magnetic flux density [Wb]
Br	Remnant magnetic flux [T]
$B_{Sat}(NO15)$,$B_{Sat}(VCoFe)$	Maximum magnetic flux density for NO15 and VCoFe [T]
$dq0$	Rotating coordinate system

f Flux density frequency [Hz]

$F1$ to Fn Groups in new population

f_w Coil filling factor

g Air-gap size [mm]

h Heat transfer coefficient [Wm^{-2}k^{-1}]

H_c Magnetic coercivity [A/mm]

I Phase current [A]

i_{od},i_{oq} Direct and quadrature torque generating current [A]

i_d,i_q Direct and quadrature current [A]

J Current density [A/m^2]

K_{eddy} Eddy losses coefficient

K_{exci} Excitation losses coefficient [W]

K_{hyst} Hysteresis losses coefficient

l_{cu} Length of one coil loop [m]

L_d,L_q Direct and quadrature inductance [H]

l_m Magnet length [mm]

L_{motor} Motor's depth [m]

P_{loss} Core, copper and PM losses [W]

l_t Teeth length [mm]

m Number of phases

N Number of individuals

n Number of objectives

N_{par} Number of coil parallel wires

np_{rotor} Number of poles in the rotor

N_{turns} Number of coil turns

p_{copper} Copper density losses [W]

p_{core} Core density losses [W]

P_{out} Useful power output [W]

P_t	Pareto optimal front
Q_t	Children population
R_{Fe}	Iron core resistance [Ω]
R_{motor}	Motor's outer radius [m]
r_r	Rotor radius [mm]
R_s	Phase winding resistance [Ω]
r_s	Shaft radius [mm]
R_t	New population
T_{amb}	Room temperature [$^\circ$ C]
T_c	Curie temperature [$^\circ$ C]
T	Torque [Nm]
T_{EM}	Electromagnetic Torque [Nm]
T_{REL}	Reluctance Torque [Nm]
T_s	Maximum surface temperature [$^\circ$ C]
u_d,u_q	Direct and quadrature Voltage [V]
V_{core}	Core volume [m^3]
w_m	Magnet Width [mm]
w_s	Stator outer ring width [mm]
w_t	Teeth width [mm]

Acronyms

AC Alternating Current

DC Direct Current

EM Electrical Machine

EV Electric Vehicle

FEM Finite Element Method

FeSi Silicon-Iron alloy

FST Formula Student Técnico

HEV Hybrid Electric Vehicle

IM Induction Machine

IPMSM Interior Permanent Magnet Synchronous Machine

NdFeB Neodymium-Iron-Boron

NEDC New European Driving Cycle

NiFe Nickel-Iron alloy

NSGA-II Non-dominated Sorting Genetic Algorithm II

PM Permanent Magnet

PMSM Permanent Magnet Synchronous Machine

SMC Soft Magnetic Composites

SPMSM Surface Permanent Magnet Synchronous Machine

SRM Synchronous Reluctance Machine

VCoFe Vanadium-Cobalt-Iron alloy

WEDM Wire-Electrical Discharge Machining

Chapter 1

Introduction

1.1 Motivation

Electric Vehicle (EV) is today present in the motor-sport environment, with the adoption of hybrid systems in Formula 1 and the development of Formula E exclusively for electric race cars. These competitions provide an opportunity to test and validate state-of-the-art technologies and to analyse the possibility of integrating them into passenger's road cars. Within this context, this project aims to design and optimise a spoke-type Interior Permanent Magnet Synchronous Machine (IPMSM) for a vehicle of Formula Student Técnico (FST) competitions with a non-conventional material as magnetic core material to contribute to the research and development of high-performance Electrical Machine (EM) and Electric Vehicles (EV).

The focus on increasing efficiency and specific power in new EM's technologies is a continuous quest within the research and industrial communities. With the development of new approaches to the EM's design and manufacturing, higher efficiency and lighter EMs are now reachable. This led to great advantages in applications where weight, volume and efficiency are key aspects, as in traction applications of electric mobility and transportation. With this purpose, an approach to produce optimised EMs was done, applying new soft-magnetic materials to the EM's magnetic core to spread current electromagnetic limits and optimising existent topologies.

Vanadium-Cobalt-Alloy (VCoFe) is the soft-magnetic material tested in this project to be compared against the typical Silicon-Iron (FeSi) alloy. VCoFe is defined by a high saturation point of 2.2-2.4 T [1] and, bearing this, it has been emerging as one potential candidate to expand current electromagnetic limits of EMs, regarding its power density and efficiency [2]. Although, its higher magnetic densities may lead to a higher contribution of losses and consequently, the pursuit whereas the achievable reduced core volume is enough to, for the same power, maintain higher efficiency values than the typical FeSi magnetic cores is essential. The thermal behaviour has also high influence in the motor design, not only it may determine if a design is viable or not, due to each material's withstanding temperature, but it also becomes significant as higher magnetic core losses may prevent the full use of VCoFe's high magnetic flux density.

Several studies have established benefits on using VCoFe as the magnetic core material of EMs for high-speed traction applications and aerospace applications to increase the specific-power of Synchronous Reluctance Machine (SRM) [3–5] and Permanent Magnet Synchronous Machine (PMSM) [6, 7]. Concerning EV traction applications, the use of VCoFe has been a minor success compared with FeSi, although [2, 8] account with an increase of at least 20% in torque/specific-power.

A previous FST competition car powertrain has been designed with a high-performance spoke-type IPMSM using FeSi as magnetic core material [9]. This project accomplished the manufacturing and validation of the motor through experimental testing where VCoFe is considered as a promising material to improve the performance of the FST car. The spoke-type IPMSM topology was opted for the powertrain of the FST's car since it is an advantage due to the higher concentration of magnetic flux in the air-gap, resulting in higher torque density and it aligns with the high acceleration requirement used in the racing tracks [10].

Within this topic, this work intends to analyse the impact on the performance of electrical motors using VCoFe as magnetic core material to reach a higher limit of specific power and a higher power/volume ratio.

As this is a multiphysics problem with non-linear materials and with a high number of variables and constraints, a multi-objective optimisation is done using a Non-dominated Sorting Genetic Algorithm II (NSGA-II) [11] to provide a general comparative analysis between VCoFe and FeSi materials for the application. This algorithm is used over a hybrid model of the motor where both analytical and Finite Element Methods (Finite Element Method (FEM)) are used, similar to the previous study done [9]. This approach has been proved to be a successful method in [11] taking less computational time than purely FEMs [12] while providing accurate enough results.

For this project, the introduced motor topology together with the hybrid model, offer accurate electromagnetic and thermal results as long as feasible times of computation. The motor's electromagnetic quantities are calculated with a stationary 2D FEM together with analytical expressions to estimate losses in the core and Permanent Magnet (PM)s and the estimated machine's operating temperature, which allow the optimisation of the EM and its increase of the current specific-power and efficiency limits.

1.2 Objectives

The main objective of this thesis is to contribute to the development of an electric motor for FST racing car with a new ferromagnetic alloy. This alloy is Vanadium-Cobalt-Iron (VCoFe) where its main characteristic is the high saturation point and its purpose is to be used as the magnetic core material of the motor to maximise efficiency and specific-power. Analysing the impact of this alloy on the design and implementation of electric traction motors recurring to an optimisation algorithm is an aim for this project.

With this purpose, a group of objectives was set to be achieved with this dissertation. These are the following:

- Comparison between different topologies of synchronous traction motors.

- Choice of optimal topologies for electrical vehicles.
- Develop a hybrid analytical/FEM thermal and electromagnetic model to calculate the performance of multiple IPMSM geometries with low computational time.
- Use of multi-objective optimisation algorithms to reach the best possible IPMSM design, for multiple materials. (VCoFe and FeSi)
- Overall performance comparison of the optimised geometries between the VCoFe and the FeSi one.

1.3 Thesis Outline

The present dissertation contains six chapters. Subsequent to this introduction, the five following chapters are presented:

- Chapter 2 - Background: A revision of the principal properties of the main EMs general types and the several soft-magnetic materials to use in the manufacturing of these is done. Particular emphasis is given to the materials and manufacturing technologies, focusing on the influence of using VCoFe alloy as magnetic core material and its main properties compared with the typical FeSi alloy in previous studies.
- Chapter 3 - Permanent Magnet Synchronous Machine Modelling: The focus in the motor's base topology and its electromagnetic and thermal model is performed. The main geometry of the motor is described along with the materials used for this topology. The B-H magnetic curves and the specific losses curves of the magnetic core materials are presented together with the characteristic of every material used in the manufacturing of the EM.

  The electromagnetic modelling is done analytically and based on a synchronous $d-q$ reference frame IPMSM equivalent circuit considering iron losses, where its main parameters are obtained using a FEM tool since a hybrid analytical and FEM is used to represent the IPMSM. A simplified thermal model is considered, where the machine is considered as a cylinder that produces heat from the Joule losses and it is a system cooled by water.
- Chapter 4 - Multi-Objective Optimisation: The concept of how the elected NSGA-II algorithm works is introduced in this chapter. The design is optimised targeting the best possible geometry to maximise the electromagnetic torque and efficiency of the studied IPMSM. The decision variables used as optimisation vector and the design constraints and their values are also detailed.
- Chapter 5 - Results: The results obtained for both VCoFe and FeSi alloys are represented as the optimised solution of the last generation arranged increasingly by its torque and compared between the two different materials. Studies regarding the preferred working area of this EM and the length of its air-gap are done.

- Chapter 6 - Conclusions: This chapter contains the major conclusions regarding the results obtained during the development of this project. The use of VCoFe material for this particular application and similar ones is discussed. Summarising a set of conclusions and the main contributions of this dissertation. It also includes some suggestions and considerations for future development in the study of specific applications for the use of VCoFe as magnetic core material.

Chapter 2

Background

A technical overview of the topic of Electrical Machines (EM) is done in this chapter. Starting with identifying the main EMs general types, and types adopted for traction such as induction machines, synchronous reluctance machines and permanent magnet syhnchronous machines.

Several motor core materials and theirs properties differences are shown. Namely, soft magnetic composites, amorphous and nanocrystalline materials and nickel-iorn, silicon-iron and vanadium-cobalt-iron alloys. A comparison between vanadium-cobalt-iron and silicon-iron regarding previous studies is done.

The section treatment of laminated materials describes briefly the post-processing machining of the materials and the considered best technique, where cutting, annealing and stacking processes are deeply described afterwards in Appendix A.

Contents

2.1 Electrical Machines (EM)

EMs have a wide range of topologies, from stationary to rotating machines, from Alternating Current (AC) to Direct Current (DC), from synchronous to asynchronous topologies, as well as several kinds of various designs and manufacturing processes. This project main study focus is in EM motors that typically have the best performance for traction applications.

One of the main considerations to have, while designing traction motors for EV application, is their operation being in a highly non-linear condition such as cross-coupling and saturation. Due to required high-performance ratios, EMs are generally designed to work just below the saturation knee point of the B-H magnetisation curve, as is shown in Fig. 2.1. Following this, torque-speed profile, inverter output power capability, torque ripple requirements, total weight, cost and so on, are main points to evaluate, along with the mechanical constraints such as efficiency, vehicle mass, wheel inertia, gearbox ratio, etc.

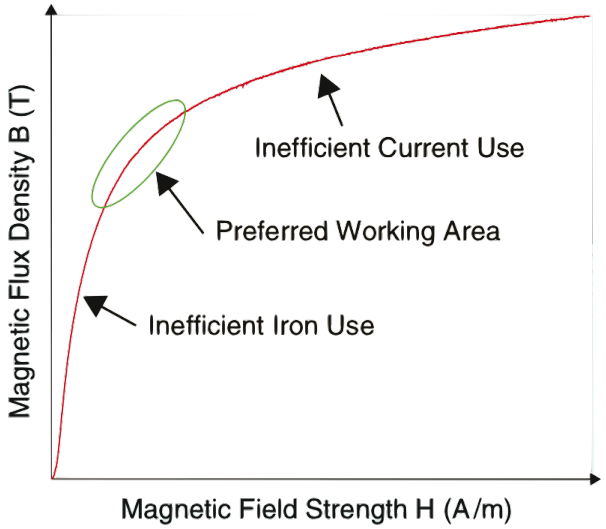

Figure 2.1: Machine operating points of the material's B-H curve [2].

2.1.1 Induction Machines (IM)

Induction Machine (IM) motors are characterised by their design without magnets, robustness, sturdiness and global availability. Industrially, field-oriented control of IMs is considered a standard. Car manufacturers appreciate these machines for safety reasons, through being naturally de-excited in case of inverter faults and for economic reasons.

Typically designed to have the lowest possible transient reactance, are able to achieve acceptable overload power curves at low speed and high torque maximum inverter's current. These machines have high efficiency at high speed but, due to copper loss, it has a wide low-efficiency region at low speed.

Nevertheless, this topology has several limitations. Due to the heat being generated both in rotor and stator side, the cooling system is a delicate matter along with the loss and energy consumption regarding the cages losses both at low and high speed. IMs have low peak power density and, for a giving rated power, the motor needs more current due to the low power factor that requires higher stator current to balance the significant Joule losses [12].

An example of a typical IM geometry cross-section, with three-phase windings in the stator and three-phase short-circuited windings in the rotor can be observed in Fig. 2.2. This particular one presents a design with 48 stator slots and 36 rotor slots. The colourful sections are where the copper windings are sited.

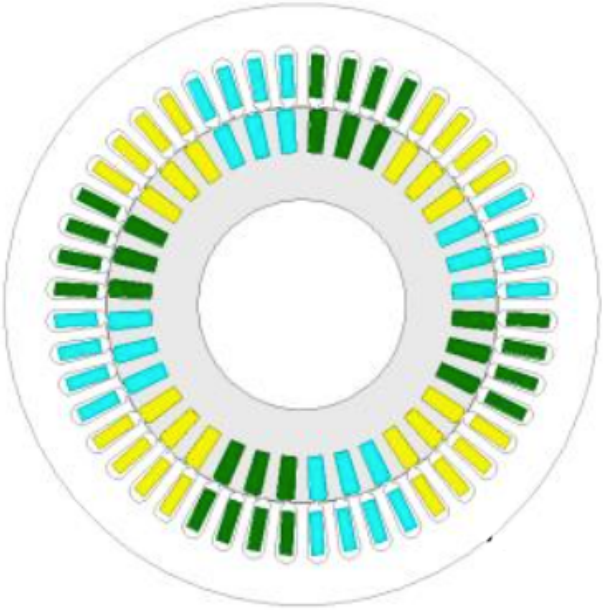

Figure 2.2: Cross-section view of an induction motor. Adapted from [12].

2.1.2 Synchronous Reluctance Machines (SRM)

SRMs are opted on harsh environment applications and fault-tolerant operation regarding being extremely robust and not depending on permanent magnets, windings nor current-conducting paths, therefore with very low rotor losses. It has a competitive power factor, inverter requirements and easy speed control without encoders even at low or zero speed operation.

However, SRM have some major challenges to the overall performance, namely high acoustic noise, serious vibration due to operating in discontinuous current, a higher number of power cables to enable independent phase on stator windings, being these with low resistance but with the need of more current to deliver the desired torque, the need of customised inverter and a low peak power density. [13]

This topology is presented in Fig. 2.3, where the rotor made of layers of magnetically soft material can be seen. These ferromagnetic layers are oriented along the stator magnetic field and follow it as it rotates.

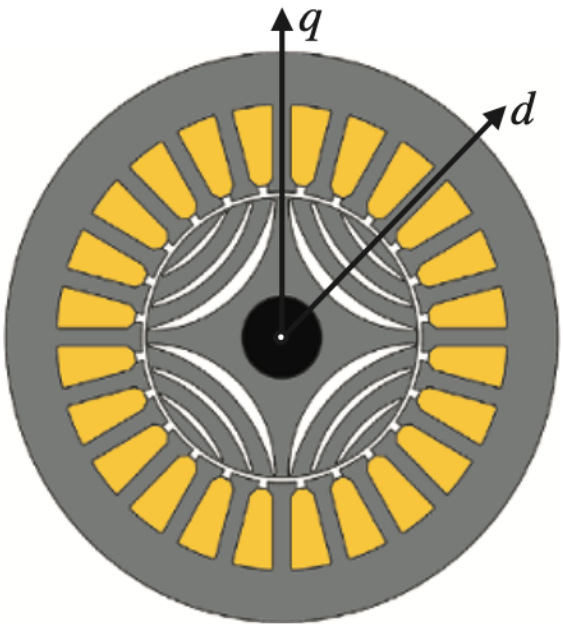

Figure 2.3: Cross-section view of a synchronous reluctance motor [13].

2.1.3 Permanent Magnet Synchronous Machines (PMSM)

PMSMs are a powerful solution for traction application dominating the traction motor market. These are designed to operate over a vast torque speed range with higher torque density, power density and efficiency, concentrating winding low resistance. It has an accurate control requiring a custom algorithm when a flux-weakening operation is required over a vast speed range, namely traction applications.

The drawback of this topology is the PM losses at high speed, despite magnet segmentation, the low number of pole pairs and their cost, regarding rare earth element price volatility due to their availability. A solution for this can be replacing the rare earth element with cheaper ferrite magnets or the use of Dy-free PMs [14].

These synchronous machine motors have two different topologies, the surface PMSM, Fig. 2.4(a), and the interior PMSM, Fig. 2.4(b), detailed below;

Surface Permanent Magnet (SPMSM)

Surface Permanent Magnet Synchronous Machine (SPMSM) are manufactured by embedding magnets in the surface of the rotor and using strong magnetism of the magnets for good motor torque and superior control. A big plus, industrial wise, is the simpler easier stator construction with concentrated stator coils, yellow coloured in Fig. 2.4(a), with very short end connections, however, the arc-shaped magnets, blue coloured in Fig. 2.4(a), can be a problem for manufacturing, adding to these the need for structural sleeves for permanent magnets retention.

The issue of this topology is the necessity of a large air-gap, the direct and quadrature axis inductance being nearly equal, limitations at overload, independently of the available inverter current and undesired permanent magnet's eddy current losses at high-speed [14].

Interior Permanent Magnet (IPMSM)

IPMSM is a type of motor where the permanent magnets are embedded inside the rotor, reducing the risk of the magnet being peeled off by centrifugal force and allowing various structures embedding permanent magnets. This magnet configuration is seen in Fig. 2.4(b) with the colour blue.

It requires multiple flux barriers for having high saliency, however, this high saliency comes with much larger overload torque over the entire speed range and a safer electromotive force in uncontrolled generator operation. These machines, with distributed windings and high saliency, typically do not generate a significant amount of heat in the rotor and have little sensitivity to the temperature of the permanent magnets, leading the main motor losses to occur in the stator which can be easily cooled by multiple cooling systems.

IPMSM biggest advantage in vehicle applications, like traction motors, is the high-speed and overall performance, at any load and speed, given that it is a high saliency machine maximised by appropriate design. [12]

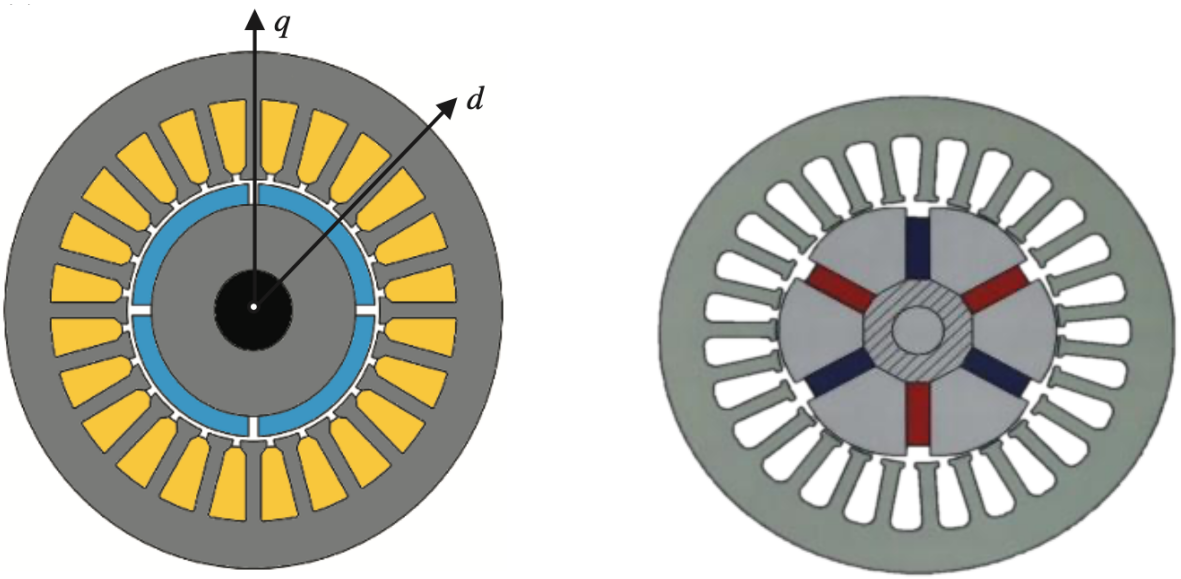

(a) Surface permanent magnets [13]

(b) Interior permanent magnets [15]

Figure 2.4: Cross-section of PMSM synchronous machines.

2.1.4 Electrical Machine Types Comparison

Energy loss comparison for an IM, IPMSM and a SPMSM has its results presented in Fig. 2.5(a). These three motors were compared in terms of motor energy consumption, with reference to the New European Driving Cycle (NEDC) presented in Fig. 2.5(b), which consists of four repeated european urban driving cycles and an extra-urban driving cycle.

IPMSM and SPMSM motors demonstrate identical results in the first part of the cycle, from 0 to 800s, yet the higher vehicle speed penalises SPMSM. Although both IM and IPMSM have a constant rate of energy consumption over the lower speeds, IM has undoubtedly higher motor losses.

Being the frequent starts and stops, in the low-speed region, characteristic of this project, IPMSM offers the best comparison results.

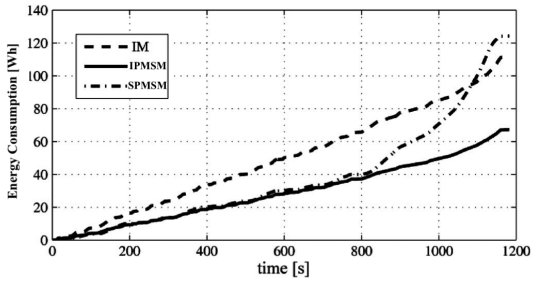

(a) IM, IPMSM and SPMSM comparison. Adapted from [14].

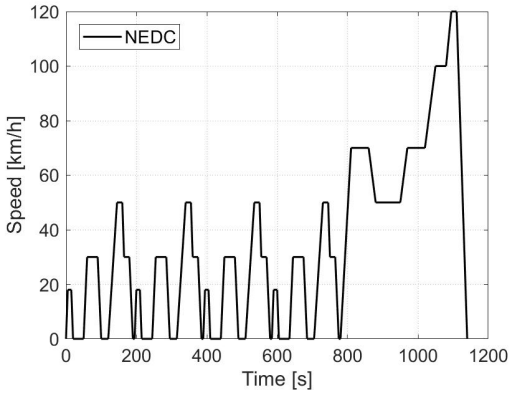

(b) NEDC

Figure 2.5: Energy loss comparison for an IM, IPMSM and a SPMSM and the NEDC representation.

Furthermore, in Fig. 2.6 the efficiency maps for a 12/8 IPMSM, 48/36 IM and a 12/8 SRM are presented in figures 2.6(a), 2.6(b) and 2.6(c) respectively, showing the region where the highest efficiency locates for each machine type [12]. The efficiency calculation is defined as:

$$\eta = \frac{P_{out}}{P_{out} + P_{loss}} \tag{2.1}$$

Where P_{loss} includes core, copper and PMs losses and excludes frictional and mechanical losses. These losses calculations are studied in section 3.2.3, Losses Calculation.

Fig. 2.6(a) shows the efficiency map for a 12 stator slot with 8 rotor poles IPMSM, where the highest efficiency is 98% located around 2000 rpm and between 20 Nm and 90 Nm, due to its concentrated winding structure, favoured to EV and Hybrid Electric Vehicle (HEV), as most frequently operation lies between low and medium speed range. However, at speeds above 5000 rpm, 12/8 IPMSM loses this advantage due to the penalty from PMs eddy current losses.

For a 48 stator slot with 36 rotor slots IM, Fig. 2.6(b) shows the efficiency map where efficiency of 96% can be achieved only at higher speeds and underestimating core losses, since below base speed and near peak torque region, efficiency can be as low as 60%.

In Fig. 2.6(a) it can be observed that, for a 12 stator slot with 8 rotor poles SRM, the maximum efficiency 95% appears only after 3800 rpm around 100 Nm, in medium torque region [12].

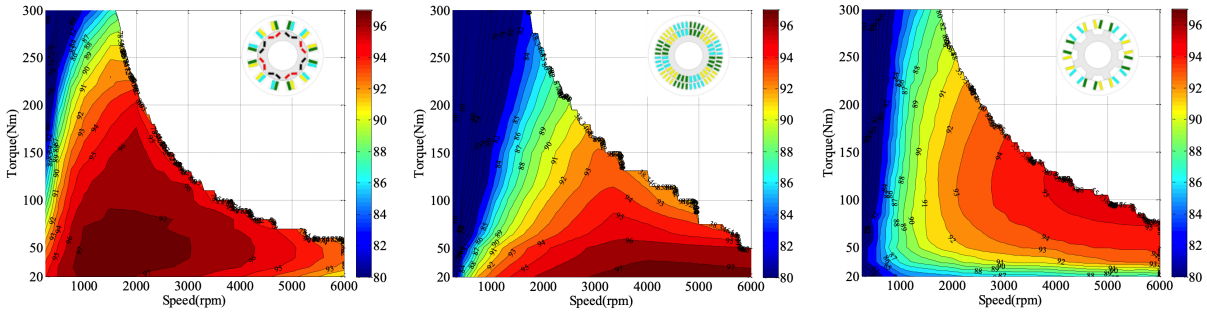

(a) 12/8 IPMSM. (b) 48/36 IM. (c) 12/8 SRM.

Figure 2.6: Efficiency maps [12].

To reinforce the results shown in the efficiency maps of Fig. 2.6, a detailed comparison of loss and efficiency at typical operating points is given in Table 2.1.

			12/8 IPMSM			
Torque [Nm]	**Speed [rpm]**	**I_d/I_q [A]**	**Core loss [W]**	**PM loss [W]**	**Copper loss [W]**	**Efficiency [%]**
30	3000	-21/16.2	161.3	37.4	61.4	97.23
50	1000	-10.2/30.1	65.5	4.2	87.9	96.99
50	5000	-65.4/23	298.5	651	418.1	94.89
300	1500	-149.2/222.4	221.4	182.3	6238	87.31
			48/36 IM			
Torque [Nm]	**Speed [rpm]**	**I_d/I_q [A]**	**Core loss [W]**	**Rotor copper loss [W]**	**Stator copper loss [W]**	**Efficiency [%]**
30	3000	16.2/34.2	97.6	95.1	121.5	96.83
50	1000	24.2/51.3	35.9	214.9	273.8	91.04
50	5000	11.1/75	110.8	458.1	488.7	96.25
300	1500	108.2/44.6	74.2	5019.1	6083.1	79.02
			12/8 SRM			
Torque [Nm]	**Speed [rpm]**	**I_{peak} [A]**	**Turn on-turn off electric angle**	**Core loss [W]**	**Copper loss [W]**	**Efficiency [%]**
30	3000	60	0-120	886.2	163.6	90.99
50	1000	80	0-120	379.1	282.9	88.47
50	5000	80	18-138	1346.2	296	93.8
300	1500	350	25-145	1019.2	6222.7	86.13

Table 2.1: Comparison of loss and efficiency at typical operating points for an IPMSM, IM and a SRM. Adapted from [12].

To obtain fast and efficient access to the energy improvements of electric motor systems, studies for three-phase electric motors with premium efficiency standards, regarding new regulations mandating the energy labelling of products, have been under process. In Fig. 2.7, where IE3, IE4 and IE5 stands for standard, super-premium and ultra-premium efficiency motor technologies for 37 kW, respectively, the losses between IM and PMSM are shown and it can be observed that the overall losses for the PMSM are lower.

Super-premium efficiency IM are reachable and feasible for small, medium and large sizes with already several prototypes made. Regarding the ultra-premium efficiency, this type of machine is not feasible at the moment. Even though, for large rating motors nano-crystalline core materials and windings by carbon nanotubes, with higher conductivity, will show possibilities of reducing iron losses and winding losses dramatically in the near future.

For SRM, the super-premium efficiency is reachable for small and medium-size motors. Some manufacturers have already existing prototypes, yet with the power factor lower than for IM. Ultra-premium efficiency SRM is seen to be feasible for small and medium rated motors applying technology as much thinner high-grade steel, increasing winding fill factor and better cooling with good thermal conductivity

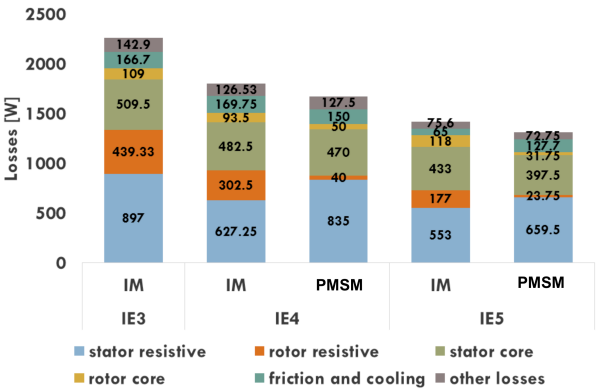

Figure 2.7: Losses for the 37 kW motor for efficiency classes. Adapted from [16].

material. However, for both efficiency standards, it may not be possible to reach large size motors without increasing the frame size due to many technical issues about reducing starting current, mechanical noise and vibrations.

PMSM is definitely reachable, both for super-premium and ultra-premium efficiency standards, for the small and medium-size. There is, at the moment, a variety of manufacturers that already have prototypes and even commercially available PMSM with these efficiency standards. Large PMSM are feasible with some issues concerning the cost of the PMs.

There are also motor types which are not suitable for some sizes as it would just be too expensive or would not even reach the desired efficiency with the existing state of the art technology.

2.2 Motor Core Materials

Material selection is a key factor in the performance of the machines. The search for new electromagnetic materials to spread the current electromagnetic limits of EMs is a constant state-of-the-art challenge. The most adequate choice of the core material is the one that maximises the power density while minimising the core losses.

Every physical aspect of the machine, from cost to weight, volume, efficiency, core losses, etc. is heavily dependable on the core material, alongside with the thermal limits. The thermal aspects limit the output power of the EM and, to correctly design an EM, the core material requires an extremely well selection to deliver the required electromagnetic and thermal model.

Low coercivity, high saturation points, low remanent magnetisation, high initial permeability, low losses, low noise and vibration harshness are desirable characteristics of that same materials.

In Figure 2.8 are represented the characteristic curves of the magnetic properties, with the specific iron losses at 50 and 400 Hz, of the studied electromagnetic materials, being these ones soft magnetic composites, nickel-iron, silicon-iron and vanadium-cobalt-iron. We can clearly observe the higher magnetic saturation values for VCoFe on both figures, followed by different compositions of FeSi. Regarding iron losses, the highest values are for Soft Magnetic Composites (SMC). Furthermore, this aspects will be detailed in the following sections.

Also in table 2.2, a brief description of these materials is presented, ranked descendingly based on their general market price for fully finished lamination sheets.

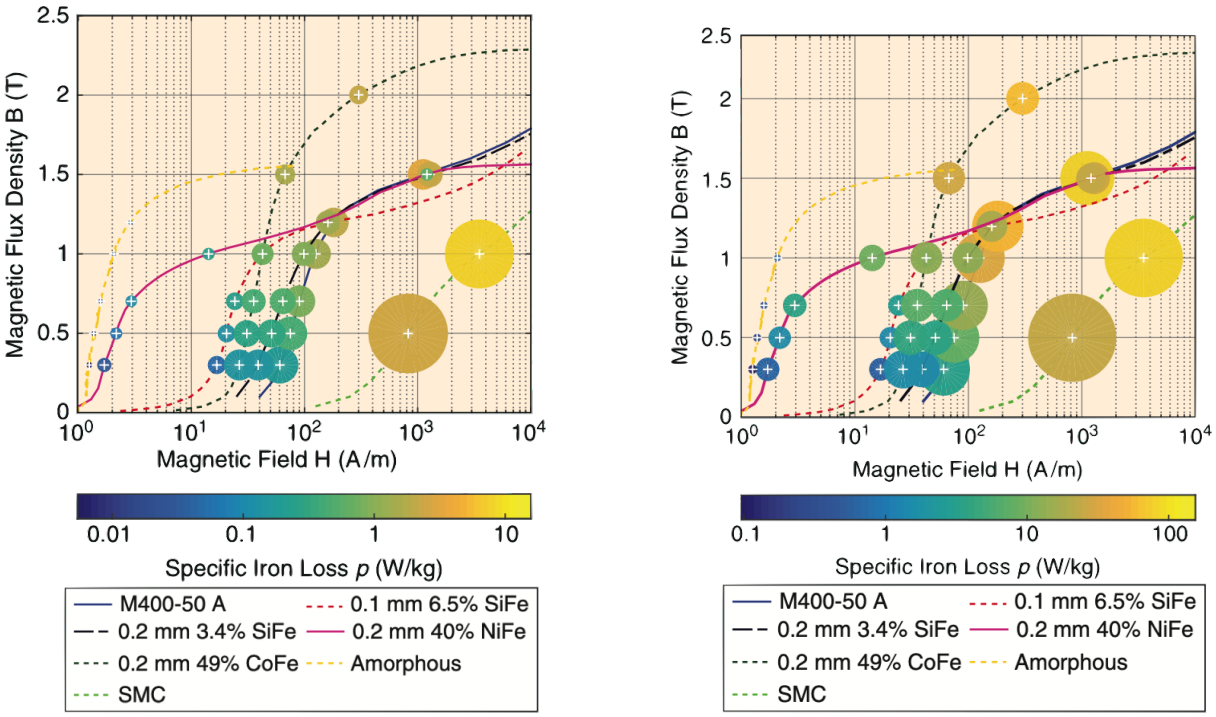

(a) Iron losses at 50Hz.

(b) Iron losses at 400Hz.

Figure 2.8: The loss-to-squared flux-density factor for typical electrical machine materials with the specific iron losses at 50 and 400 Hz [2].

Material Type	Material Composition	Sheet Thickness [mm]	Flux Density at 0.8 kA/m [T]	Flux Density at 2.5 kA/m [T]	Resistivity [$\mu\cdot$cm]	Material Density [g/cm^3]
VCoFe	49% cobalt, 49% iron, 2% V	0.2-0.5	2.1	2.23	40	8.12
Nickel-Iron alloy (NiFe)	40% nickel, 60% iron	0.1-0.5	1.44	1.48	60	8.2
High-Silicon-content FeSi	6.5% silicon, iron balanced	0.1-0.2	1.29	1.4	82	7.49
Thin non-oriented FeSi	3% silicon, 0.4% aluminum, iron balanced	0.1-0.3	1.15	1.63	52	7.65
Non-oriented FeSi	1–3% silicon, iron balanced	0.35-1	-	1.64	20-60	7.6-7.8
Amorphous Iron	20% (silicon and boron), 80% iron	0.025	1.55	-	130	7.18
SMC	<1% lubrication, iron balanced	Solid Material	0.71	1.22	20000	7.57

Table 2.2: Typical magnetic materials used in electrical machine cores [2].

2.2.1 Soft Magnetic Composites (SMC)

SMC are formed by very small, isolated iron ferromagnetic particles, from different types of iron or iron alloys, coated with an electrically insulating layer. The core is powder compacted and can be formed into complex desired shapes through powder metallurgy. Consequently, one of the main advantages of the powder is the possibility of three-dimensional magnetic circuit design and specially customised machine geometries. On the other hand, these arbitrary geometries are built by a compacting process to achieve an uniform pressure and an equally distributed material density, therefore the strength of these and the mechanical resistances are lower than laminated alloys [2].

From the electromagnetic point of view, even though it presents a very high resistivity, and due to the

material nature being of small particles, leading to low eddy current losses, this material does not have the best performance considering its moderately low permeability ($\mu_r \approx 10^3$) and flat B-H magnetisation curve with a relatively low saturation point ($B_{sat} \approx 1.5$ T) at typical magnetic field strengths in EMs. This effect is visualised in Fig. 2.9, where a non-oriented FeSi with around 3% of silicon (3 wt%) lamination and two SMC cores with different densities are compared.

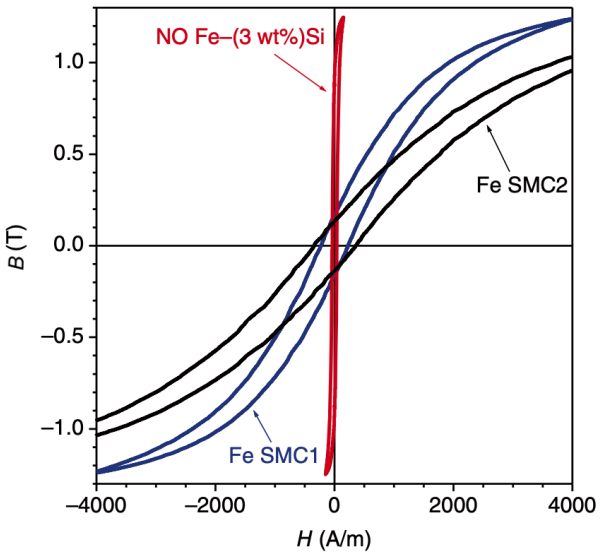

Figure 2.9: DC hysteresis loops taken at peak polarisation [17].

Suitable exploitation by the design of the available three-dimensional flux geometries can be effective in achieving improved efficiency and reduced volume in EMs. It is possible to adopt rounded teeth, allowing a higher slot filing, and tighter and shorter winding. Transverse flux and axial flux machines successfully benefit from reducing the length of the windings, low copper losses and reduced volume [17].

SMC uses are preferable on EMs where a three-dimensional flux distribution has advantages and on high economic significance solutions.

2.2.2 Amorphous and Nanocrystalline Material

Amorphous magnetic materials and nanocrystalline are produced by melt spinning contrasting with the standard hot and cold rolling procedures for forming the steel sheets. The rapid cooling process when the molten alloy touches the cold wheel surface fixes the iron molecules forming the amorphous structure without any crystalline order in the material, providing a higher resistivity. The thickness and width are limited by equally distributed dripping and cooling properties during the manufacturing process. It can be performed in air, inert gas or vacuum. [2]. This process is visualised in Fig. 2.10.

In the EM application, the common composition of amorphous materials is boron, iron, silicon and phosphorus. Usually, boron-based materials are amorphous structures with typical application areas on electronics and sensor, being boron the biggest weight of the material cost, and iron-based materials are nanocrystalline structures used in premium distribution transformers, small-high speed applications and

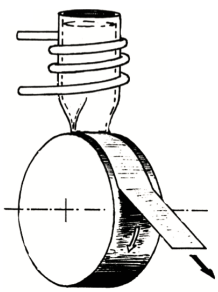

(a) Planar flow casting

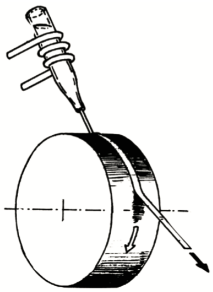

(b) Chill block melt spinning

Figure 2.10: Preparation of soft magnetic ribbons by means of rapid quenching from the melt [17].

special geometries for segmented modular machines. These amorphous structures enable reaching high values of electrical resistance and low values of coercivity (≈0.2 A/m), being an interesting solution for high-frequency applications and to compete with conventional crystalline alloys [18]. A graph comparing amorphous and nanocrystalline material's coercivity, in red and green respectively, with standard crystalline material, in blue, versus their magnetic saturation, can be seen in Fig. 2.11.

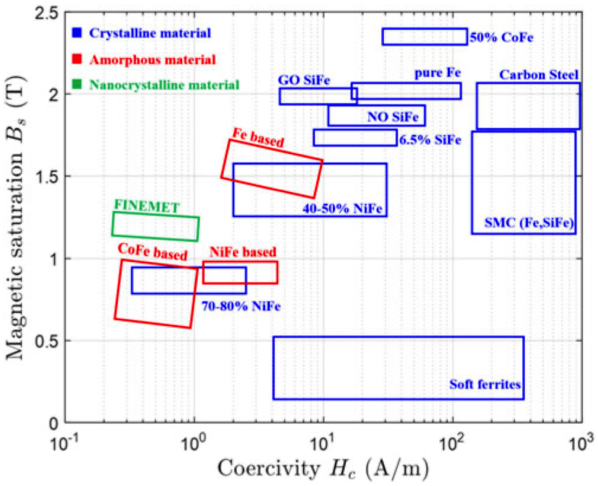

Figure 2.11: Magnetic saturation flux density versus magnetic coercivity for typical soft magnetic materials [3].

Amorphous magnetic materials and nanocrystalline materials have advantages at their very low iron losses due to their very thin foil structure, typically 0.025 mm, and low manufacturing process costs.

Although having great mechanical endurance, amorphous materials main drawbacks are their mechanical brittleness, making the handling difficult during machine core assembly process, therefore, it is typically available in the market as ready-to-use products, and with low saturation point (B_{sat} ≤1.3 T)[3].

2.2.3 Nickel-Iron (NiFe)

NiFe lamination applications are mainly on small high-speed machines, since iron losses are a crucial factor. With this alloy is possible to manufacture laminations with low iron losses and low magnetic coercivity (H_c ≈0.3 A/m), leading to a superior relative permeability ($\mu_r \approx 10^5$) and having the lowest

Curie temperature ($T_c \approx 360^\circ$ C). Nonetheless, the small maximum flux density and low saturation point (B_{sat} ≈1 T) are disadvantageous [2]. A comparison of the magnetic properties between this material and VCoFe alloy can be observed in Fig. 2.12.

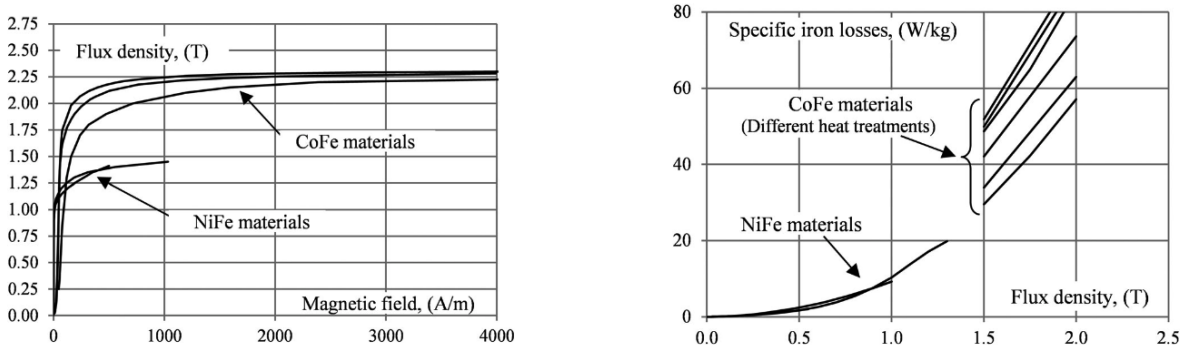

(a) Magnetisation curves of NiFe and VCoFe

(b) Typical iron losses of NiFe and VCoFe alloys at 400Hz

Figure 2.12: Magnetisation and iron losses curves of typical NiFe and VCoFe alloys [3].

Usually, nickel's content is around 40 to 50+% and the highest the nickel content is, the larger is the permeability. Although with that comes also higher electric conductivity and eddy current losses.

Cost-wise, NiFe alloys stand between the classic FeSi laminations and the more expensive VCoFe laminations.

This alloy most common applications are in electric motors where low loss requirements are critical, such as low loss aerospace applications, medical applications that have strict thermal regulation and also in non-motive devices such as resolvers [3].

2.2.4 Silicon-Iron (FeSi)

Iron alloyed with some amount of silicon is the most widely used material in EMs. The changes in the physical, mechanical and magnetic properties of iron were noteworthy with the addition of a few atomic percentages of silicon. Bringing remarkable positive effects not only on the electrical resistivity increase and on the decrease of AC losses, but just as well as in material handling and machining with yield strength increased and ceasing the final annealing temperature restriction. This addition provided the alloy with a few negative aspects such as the reduction of the saturation magnetisation, its B-H curve is presented in Fig. 2.13, smaller permeability, increasing embrittlement to materials and the fact that there is no practical way of achieving laminations with more than about 4% of silicon (4 wt%) by conventional rolling processes. Alloying with aluminium in place of silicon provides identical physical and structural effects, while not causing material embrittlement. On the other hand, aluminium is very reactive and can easily lead to oxide formation and its costlier. The use of higher manganese content leads to larger grains and thus a higher permeability, yet increases the losses [17].

FeSi alloys are available in a grain-oriented state or a non-oriented state. The first one is anisotropic magnetic material and has a different permeability in different directions, being mostly used in electrical transformers due to their unidirectional flux change in the core legs and yoke. The non-oriented state

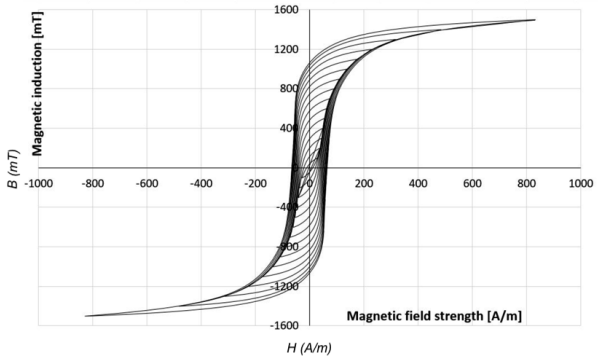

Figure 2.13: Hysteresis loops in a grain-oriented FeSi steel sheet [19].

has almost isotropic magnetic properties in all directions and is used in rotational machines since the flux direction is generally not unidirectional but changes direction rotating in the stator yoke and stator tooth tips. The majority of EMs are currently manufactured from non-oriented FeSi grades. However, grain-oriented FeSi materials are used as well as in large EMs, where the stator is constructed of several yoke parts, or in research projects investigating new EM manufacturing techniques and topologies [2]. A global market graph of magnetic materials where FeSi alloys have the biggest slice, can be observed in Fig. 2.14.

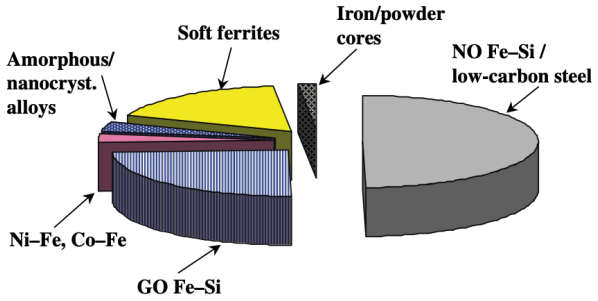

Figure 2.14: Global market slices of typical magnetic materials [17].

Due to the increased machine speeds and increased time harmonics from the drive systems, the current trends in FeSi steels are focusing mainly on iron losses reduction, with emphasis for higher base frequencies. The first trend is using high silicon-content laminations, up to 6.5%, improving the electric resistivity and thus the eddy current losses. However, drawbacks such as the reduction of maximum flux density and permeability and more complicated and expensive manufacturing processes and tooling costs are visible. The other one is thin-gauge steels, changing the thickness of the laminations from the typical 0.5 mm to 0.1-0.3 mm, resulting in higher flux densities and lower electromagnetic induction in the material, keeping the eddy current losses low at the cost of larger core assembly efforts and thus production cost. The energy loss behaviour, regarding the increase of silicon-content, can be seen in Fig. 2.15(a) whereas the energy loss, regarding different thicknesses of laminations, can be seen in Fig. 2.15(b). Common grade names take the form NOXX, where XX describes the thickness 0.XX mm as in, the afterwards described, NO15 [3].

Being the most inexpensive material on the market, alongside with its balanced magnetic properties, the FeSi alloy is the most attractive solution for the overall EMs.

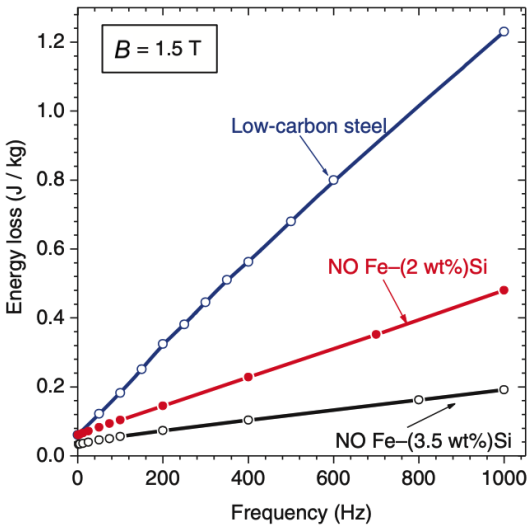

(a) Specific power loss versus magnetising frequency at peak polarisation.

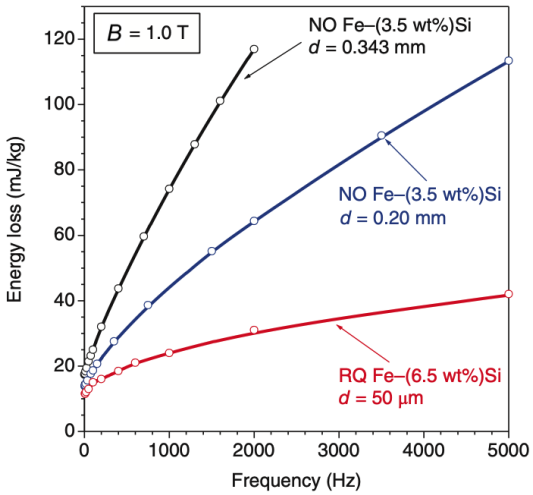

(b) Energy loss versus frequency.

Figure 2.15: Energy losses of FeSi alloys regarding silicon-content and thickness [17].

2.2.5 Vanadium-Cobalt-Iron (VCoFe)

To expand the current limits of specific-power in EMs, the addition of some cobalt to iron has allowed this to be the one with the highest saturation point, at room temperature, of all the materials described in this document (2.43 T for a 35% cobalt and 65% iron alloy) and also the most costly one, due to the expensive cobalt's price and the post-processing material required to achieve optimal properties. Cobalt percentage on the material varying from 15% to 49% brings up electromagnetic properties to material cost dilemma. The saturation magnetisation according to the cobalt-content can be seen in Fig. 2.16(a).

A common VCoFe composition for electrical materials is 48-50% cobalt, around 48% of iron and 2% vanadium leading to the highest saturation point and the best mechanical properties. Furthermore, there are different grades available and these differ in terms of other alloy additions and annealing behaviour for the same composition. The addition of a small percentage of vanadium to the alloy ($< 3\%$) provides an improvement on the material's embrittlement and electrical resistivity, keeping the high mechanical resistance, following that FeSi steels reveal low ductility which complicates the manufacturing process of alloys and lamination steels for EM applications. Although, adding a third element to the composition, brings up the drawback of decreasing the saturation point, which makes the overall of commercialised alloys having only around 2% of vanadium [20]. The saturation magnetisation variation with the vanadium-content can be seen in Fig. 2.16(b).

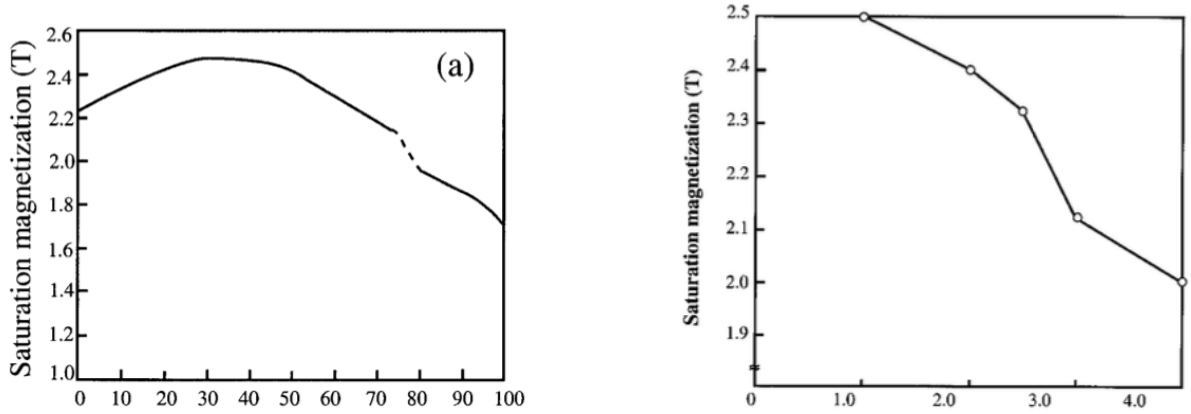

(a) Vanadium content (%) in VCoFe alloy

(b) Cobalt-content (%) in VCoFe alloy

Figure 2.16: Effect of vanadium and cobalt content on saturation magnetisation of VCoFe alloy[20].

VCoFe alloys represent a unique solution in terms of Curie temperature ($T_c \approx 950°$ C), as seen in Fig. 2.17, saturation polarisation, as seen in Fig. 2.18, and strength of lamination steels. Its electromagnetic properties are responsive to the material's purity and post-processing treatment, impacting on the coercivity and thus, hysteresis losses. Keeping the material's purity to low levels, coercivity can reach up to $H_c = 20$ A/m and relative permeability of $\mu_r \approx 2 \times 10^4$, outstanding FeSi alloys [17].

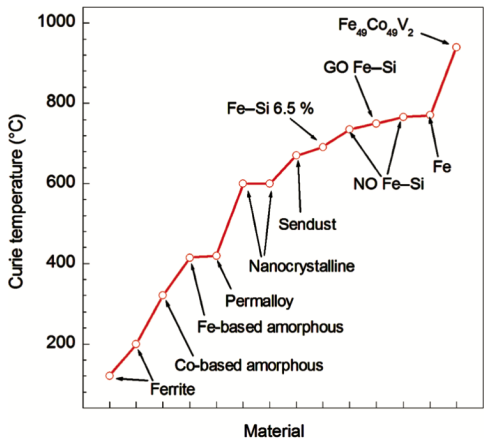

Figure 2.17: Curie temperature of the main soft magnetic materials [17].

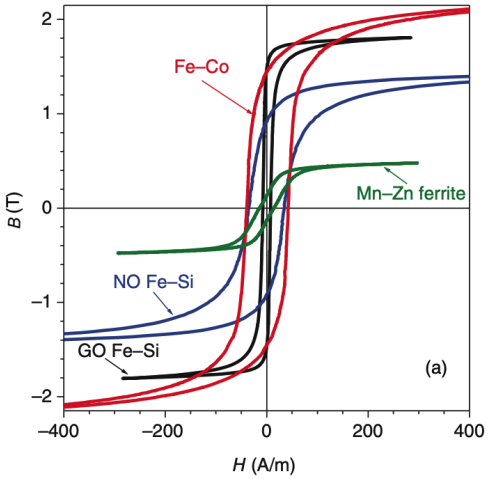

Figure 2.18: DC hysteresis loops in different soft magnetic alloys [17].

With a major maximum flux density, VCoFe alloy enables to design EMs that are significantly reduced in size and weight, leading to very high power densities. This reveals a useful number of applications where volume performance versus weight is critical and high working temperature may be required. Likewise, machine cores for aviation and space applications, where the lighter weight compensates for the higher price, magnetic bearings, flywheel energy storage systems and power generation systems at high rotational speeds. As the goal of this project, VCoFe alloy laminations are also used as specialised electric and hybrid systems in motor-sport applications, where the overall performance outweighs the cost concerns [2, 3].

2.2.6 Vanadium-Cobalt-Iron and Silicon-Iron Comparison

VCoFe alloys have been emerging on the applications for EMs. Since this alloy is characterised by higher magnetic saturation points, but also higher core losses and higher cost, there are continuous studies comparisons between VCoFe and FeSi overall performance.

Multiple of these studies have identified the potential of using VCoFe to increase the specific-power of EMs and, several of them, are specified below.

Induction Machines (IM)

In [21], two high-speed induction motors (20 kW, 30000 rpm) were built with VCoFe and FeSi. A slight efficiency increase for the VCoFe motor was observed, resulting from the higher temperature values. However, the advantages regarding the cost difference versus overall performance found themselves unclear.

Synchronous Reluctance Machines (SRM)

In [22], the authors came to the conclusion, by analysing the impact of switching FeSi to VCoFe on a high-speed SRM (300 kW, 100000 rpm), that there is a mass reduction of 30% and efficiency improvement from 40% to 90%.

The authors of [23] present the enhancement of efficiency of high-speed SRM designed with VCoFe alloy and with conventional non-oriented FeSi. It is shown that a VCoFe based SRM achieves higher efficiency compared with a FeSi based design. The authors do not present any power density or weight comparison in their results.

In [24], the optimisation design of two machines with the same dimensions for different power and velocity points (0.8-8 kW, 5000-50000 rpm) stated that VCoFe alloy can outperform the typical FeSi for high-speed applications with the adequate cooling system. However, it identifies an important trade-off in the VCoFe alloys: higher magnetic-flux density levels lead to higher iron core losses, thus leading to higher temperatures.

The author of [5] investigated, experimentally, two transversely laminated SRM (5 kW, 50000 rpm) applications of an electrically-driven compressor for a two-strokes aeronautic diesel engine, having VCoFe and FeSi as different rotor lamination materials. The obtained results verify that the rotor with FeSi requires a 9% higher current value than VCoFe while the FeSi machine shows reduced torque oscillations and rotor losses. Even-though, both machines overall efficiency calculated at 50000 rpm are above 94%, the author sees a further solution to improve power factor as inserting PMs within the rotor barriers.

Permanent Magnet Synchronous Machines (PMSM)

In [8], a PMSM (28 kW), previously with FeSi alloys as core material, was prototyped replacing VCoFe both in stator and rotor. The highest saturation polarisation of more than 2.3 T was obtained by using VCoFe laminations and a maximum torque increase of at least 25% was indicated.

Past works in Técnico Lisboa, Energy Scientific Area

A single-phase transformer was tested experimentally using VCoFe alloy by the author of [25], where he suggests that, for higher frequency/speed, VCoFe's higher density losses may result in lower efficiencies and higher temperatures, thus limiting the achieved specific-power, if the machine's magnetic core is not optimised.

2.3 Treatment of Laminated Material

Following the choice of the best suitable material for the purpose goal, the manufacturing and post-processing various procedures step in concern. Multiple types of technologies and approaches are available in the market, each of them with different advantages, disadvantages and price ranges. The manufacturing process to obtain a laminated alloy requires processes to cut the magnetic sheets to the required design, to go through an annealing process and to stack them assembling all the different sheets forming the stator and the rotor. To make use of the optimum magnetic and mechanical properties, each of these steps can be made using different types of technologies and different processing orders.

These steps, during the manufacturing of the laminated materials, are described in Appendix A, where an in-depth characterisation of the most common processes for each step is done

Fig. 2.19 exhibits the B-H curves of the VCoFe sheets for the different sequences of annealing combined with stamping and Wire-Electrical Discharge Machining (WEDM) cutting processes. Significantly superior soft-magnetic characteristics are noticeable in the annealed material, where the stamping followed by the annealing presents the best results for the material treatment. It is also noticeable that the characteristics of the material are almost re-established after annealing and the best magnetic properties can be achieved.

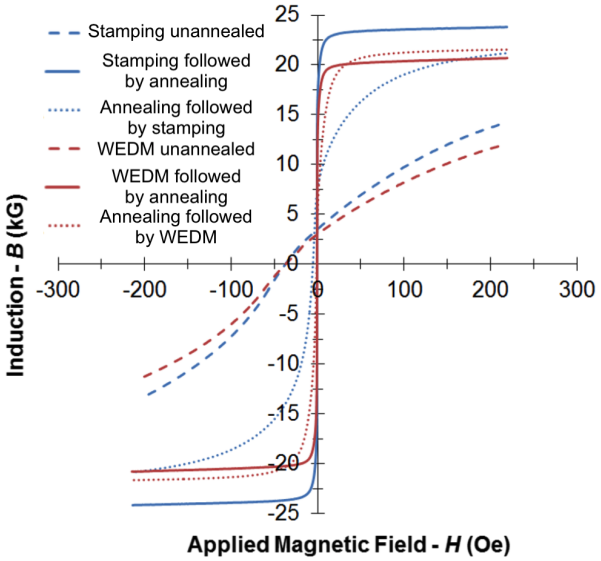

Figure 2.19: B-H curves of the VCoFe sheets annealing, stamping and WEDM processes combinations [1].

Chapter 3

Permanent Magnet Synchronous Machine Modelling

A detailed methodology for the study of an Electrical Machine (EM) is shown here based on an Interior Permanent Magnet Synchronous Machine (IPMSM), as well as the description of all the different components and characteristics.

The section base topology aims to explain the procedure regarding the geometry and design of the machine, the various motor materials used in every domain of the machine and the winding configuration elected for this study.

The contribution of this thesis to the analysis of the electromagnetic modelling is described. The coordinate system used in the study, the equivalent $d-q$ - circuit, where magnetic saturation effects are included through an equivalent resistance and lumped parameters and how the FEM is used to estimate results are detailed. An auxiliary script coupled with the FEM is used to calculate the EM's losses analytically.

Furthermore, the thermal model used to estimate the machine's temperature for a specific steady-state operation point is also presented.

Contents

3.1 Base Topology

To start designing the base topology of the EM, its geometry and properties are studied as characteristic dimensions, as well as its motor materials and windings configuration. The characteristic dimensions of each part of the motor's magnetic core will be considered as decision variables for the optimisation process.

3.1.1 Geometry

The EM is based on a spoke-type IPMSM with a flux-concentrating rotor design, with PMs magnetised alternately, along the angular coordinate. This base geometry is designed for demanding high-performance requirements and it was developed and validated for a 20 kW 8000 rpm IPMSM in [9]. In Fig. 3.1 a cross-section of the proposed geometry can be observed where the PMs are presented in gold colour, the copper windings are presented in bronze colour, the air is presented in light blue colour and the magnetic core material is presented in grey colour.

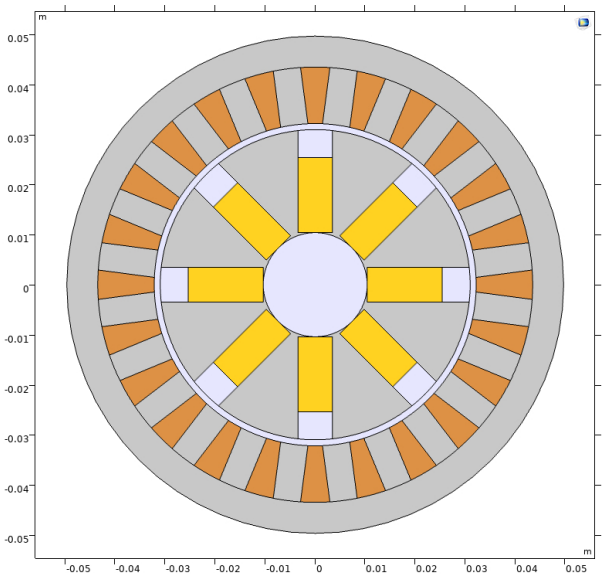

Figure 3.1: Interior permanent magnet synchronous machine model cross-section geometry.

The dimensions of the different components of the motor will determine the final motor design, being these used as decision variables in the optimisation process to maximise the IPMSM's torque and efficiency. These dimensions are the number of poles, number of phases, rotor radius, r_r, shaft radius, r_s, magnet width, w_m, magnet length, l_m, teeth width, w_t, teeth length, l_t, stator outer ring width, w_s, and air-gap size, g. These dimensions are presented in Fig. 3.2.

Considering that the competition car has four identical motors mounted in the suspension of each wheel, the outer dimensions are limited to the available space. The maximum outer radius and length are equal to 50 mm and 80 mm, respectively.

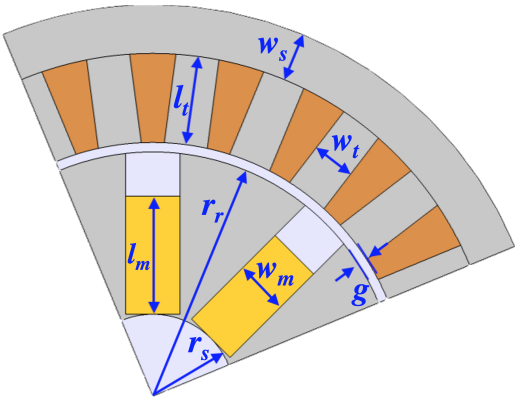

Figure 3.2: Geometry dimensions.

3.1.2 Motor Materials

The material selection for the different sections of the motor must be done to maximise the mechanical output power and, at the same time, to promote the machine's reliability.

The reliability of the developed motor will be achieved when the rotor can withstand the centrifugal forces and the electromagnetic materials operate securely in the operation temperature.

The production of heat coming from the different types of losses highly influences the motor temperature. The main temperature limiting factors are related to the withstanding temperature of the copper winding's insulation and of the PMs. The higher the temperature they can withstand, the higher will be the available peak and continuous torque and power.

The materials used on the motor and their properties considered in the electromagnetic and thermal models are defined below.

Air

With the motor divided into two parts, rotor and stator, an air-gap should be defined between them. From the magnetic point of view, this air-gap should be as small as possible to reduce its magnetic reluctance and facilitate the transmission of energy between the stator and the rotor and to reduce the reactive power. A wide air-gap could have a negative impact on the efficiency and performance of the motor.

From the mechanical point of view, the air-gap should be large enough to avoid contact between the stator and rotor, even in the presence of torque ripple, loose bearings or movement that results from deflection during operation. Because of this, the minimum air-gap length value was set to 1mm, defined empirically based on the feedback provided by the FST (the value used in their first motor).

In the FEM model, the air domain was defined with a unitary relative magnet permeability, $\mu_r = 1$ and a null electric conductivity, $\sigma_{air} = 0$ S/m.

The parts of the machine corresponding to the air material are represented in Fig. 3.1 in light bluer colour. The shaft of the machine is also considered as air in the FEM analysis since it is always manufactured with stainless steel, a non magnetic material that can be magnetically compared with air.

Copper

Copper is selected as material for the stator windings. This material has excellent conductivity, malleability and corrosion resistance. Its physical properties used in the model are described in Table 3.1 and the parts of the machine corresponding to the copper material are represented in Fig. 3.1 in colour bronze.

Properties [Units]	Copper
Equivalent electrical conductivity [S/m]	5.998×10^7
Thermal conductivity [W(m.K)]	400
Temperature coefficient of resistivity [1/K]	0.0039
Density [kg/m^3]	8960

Table 3.1: Properties of Copper.

Neodymium-Iron-Boron (NdFeB)

Neodymium-Iron-Boron (NdFeB) is the base material for the PMs since it is a hard magnetic material capable of retaining high values of remnant magnetic flux density and presenting a high demagnetisation temperature.

Due to their properties, NdFeB PMs are today the most competitive PMs used in high-performance EMs.

In this model, NH40 grade with remnant magnetic flux B_r =1.2 T was considered and its main properties are described in Table 3.2. The parts of the machine corresponding to the Neodymium material are represented in Fig. 3.1 in gold colour.

Properties [Units]	NdFeB
Relative magnetic permeability μ_r	1.05
Remanence [T]	1-1.4
Coercivity [kA/m]	750-2000
Energy product (B-H)$_{max}$[kJ/m^3]	200-440
Saturation H [kA/m]	$>$2400
Maximum Curie temperature [$^\circ$C]	310-400
Density [Kg/m^3]	7400

Table 3.2: Properties of Neodymium.

Silicon-Steel Alloy (FeSi)

Silicon steel (NO15) is one of the possible magnetic core materials that can be used in the motor's rotor and stator. It is known as a soft magnetic material that is easy to magnetise and demagnetise along with low hysteresis losses. The main characteristics to consider are the saturation and the permeability that have a high influence on the maximum magnetic flux density and core losses, thus influencing the machine overall efficiency and power-density.

The material chosen for the model is *Silicon Steel NGO 35JN200* and its main properties can be seen in Table 3.3. The parts of the machine corresponding to the NO15 material are the core of the machine, represented in Fig. 3.1 in silver colour.

This magnetic core material is characterised by its respective B-H magnetic curve and specific loss curve obtained for a nominal frequency of 400 Hz, presented in Fig. 3.3, for laminations of 15 mm thickness. These curves were achieved by fitting data from the manufacturer's data-sheet.

Properties [Units]	**NO15**
Magnetic saturation [T]	1.6
Losses at 50 Hz with 1 T [W/Kg]	1.08
Losses at 400 Hz with 1 T [W/Kg]	12.1
Ultimate tensile strength [MPa]	450
Density [kg/cm^3]	7650

Table 3.3: Properties of NO15.

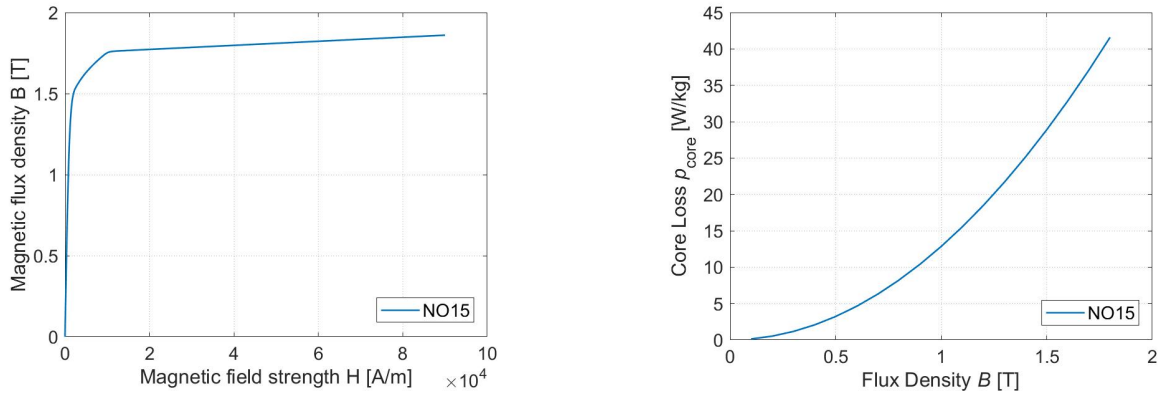

(a) B-H magnetisation curve

(b) Specific losses curve

Figure 3.3: Respective B-H magnetisation and specific losses curves for NO15.

Vanadium-Cobalt-Iron Alloy (VCoFe)

The other possible choice for the magnetic core material of the machine is the main study of this project, Vanadium-Cobalt-Iron (VCoFe), an alloy with very high saturation point, low coercive field strength and low specific core losses. It overcomes NO15, on the linear zone, in means of higher saturation points (2.2-2.4 T) and higher relative magnetic permeability. However, VCoFe prices are higher and more volatile than the NO15, and for this reason, both materials will be studied for optimisation and better performances purposes.

The material chosen for the model is *Cobalt Steel Vacoflux 50* and its main properties can be seen in Table 3.4. The parts of the machine corresponding to the VCoFe material are the magnetic core of the machine, represented in Fig. 3.1 in silver colour.

Once again, this magnetic core material is characterised by its respective B-H magnetic curve and specific loss curve obtained for a nominal frequency of 400 Hz, presented in Fig. 3.4, also for laminations

of 15 mm thickness to reach a better comparison with NO15. These curves were achieved by fitting data from the manufacturer's data-sheet.

Properties [Units]	Vacoflux 50
Magnetic saturation [T]	2.35
Losses at 50 Hz with 1.5 T [W/Kg]	1.6
Losses at 400 Hz with 1.5 T [W/Kg]	31
Ultimate tensile strength [MPa]	350
Density [kg/cm^3]	8120

Table 3.4: Properties of Vacoflux 50.

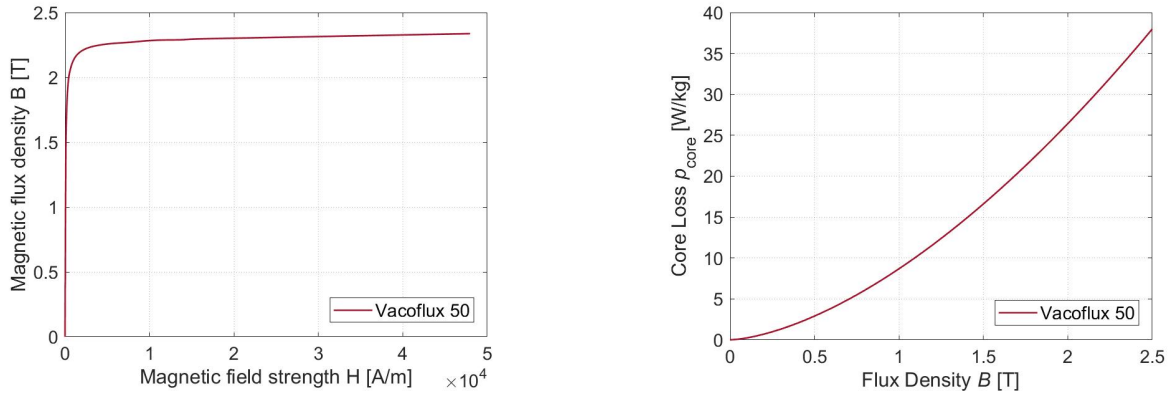

(a) B-H magnetisation curve

(b) Specific losses curve

Figure 3.4: Respective B-H magnetisation and specific losses curves for Vacoflux 50.

3.1.3 Winding Configuration

For determining the optimal winding design configuration an automated independent procedure was used combining a multi-objective genetic algorithm and the winding analysis to reach an optimal winding pattern [26]. The user merely defines variables such as number of stator slots, number of poles, number of phases and whether a single or double-layer winding is required and the procedure will determine the optimal winding layout, according to the nominal rotation speed required for the competition vehicle.

The multi-objective algorithm has as objective to maximise the fundamental field whilst also minimising the harmonic fields and maintaining electrical balance.

The fundamental magnetomotive force (mmf) establishes the quantity of flux moving between the rotor and the stator, being highly dependent on winding configuration and the length of the air-gap and having important weight on the motor torque. By minimising the harmonic fields the machine will have less torque ripple and higher efficiency consequently. The electrical balance is associated with the movement flow of the magnetic rotating waves on the air-gap.

This study and the winding configuration opted for the model was previously performed in [27]. The combinations considered were the number of stator slots being 12, 24 and 30 and the number of rotor poles being 6, 8 and 10 so that the velocity requirements for the motor are met. All combinations were

reviewed having only a single layer winding and can be consulted in Table 3.5.

Study	Fundamental	Sum of harmonics	Balanced
12 slots / 6 poles	0.574	1.790	Yes
12 slots / 8 poles	0.414	1.169	Yes
12 slots / 10 poles	0.369	2.137	No
24 slots / 6 poles	0.979	2.512	Yes
24 slots / 8 poles	0.956	0.414	Yes
24 slots / 10 poles	0.732	2.394	Yes
30 slots / 6 poles	1.501	2.630	No
30 slots / 8 poles	1.120	3.576	No
30 slots / 10 poles	0.902	2.907	No

Table 3.5: Motor winding layout results. Adapted from [27].

The chosen configuration was 24 stator slots and 8 rotor poles, minimising the sum of harmonics on 0.414 with 0.956 fundamental mmf per amp.

In the stator, a single-layer concentrated winding layout was adopted to maximise the fundamental component of the air-gap magnetomotive force wave and to simplify the manufacturing process.

The adopted winding configuration is shown in Figure 3.5.

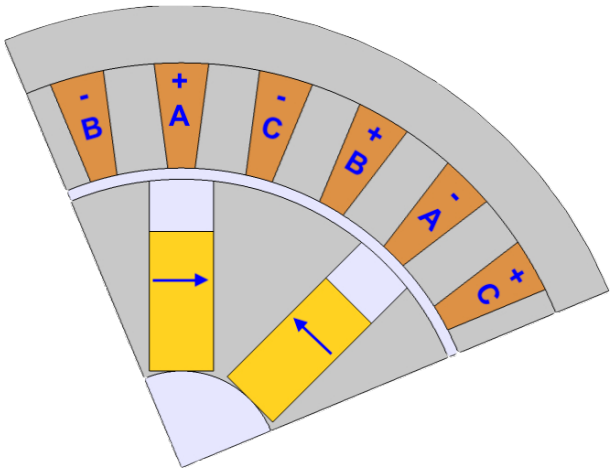

Figure 3.5: Winding Configuration.

3.2 Electromagnetic Modelling

The electromagnetic analytical modelling is based on the synchronous $d-q$ reference frame IPMSM's equivalent circuit considering iron losses, where its main parameters are obtained using a FEM tool. A hybrid analytical and FEM is used to represent the IPMSM to reduce the optimisation computational time to a feasible time. The optimisation can result in very high computational times due to its iterative process requiring a high number of simulations of the EM. This methodology will allow a good estimation of the main machine's equivalent circuit parameters of each tested geometry with a 2D stationary time simulation being used, as well as an estimate on the machine's performance for different operation points.

3.2.1 Coordinate System

Due to the continuous change in the position of the rotor concerning the stator in the machine, a steady-state scheme cannot describe this dynamic behaviour. Consequently, a different reference model, characterised by differential equations with time-varying inductances is accounted for.

Using the stationary coordinate system (abc) would result in a large set of complex equations requiring a greater effort to accomplish the dynamic analysis. Regarding this, the use of a rotating coordinate system ($dq0$) to lower the complexity of the analysis was employed. Applying the direct-quadrature-zero transformation with the synchronous speed reference frame, it was able to simplify our coordinates from three AC quantities to two DC quantities, d and q.

Axes d and q can be assumed to be rotating at the same angular speed as the space vector, resulting in constant direct and quadrature components over the time in Fig. 3.6(b).

Fig. 3.6 enables a comparison between the two reference frames where it can be observed that over the different rotor's angle, $d-q$ frame in Fig. 3.6(b), components will always be continuous quantities during steady-state, while the abc quantities, in Fig. 3.6(a) keep changing.

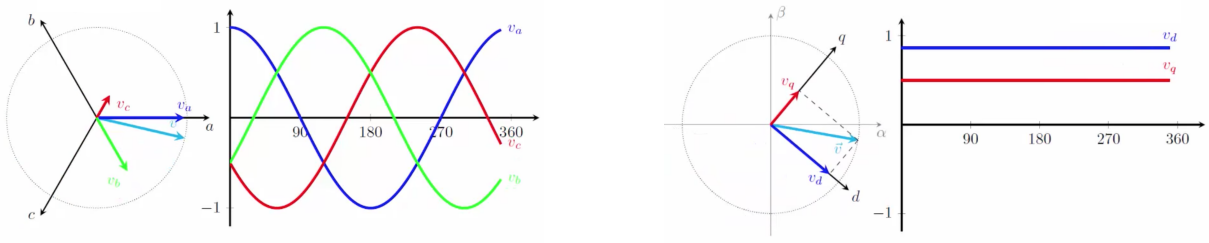

(a) abc frame

(b) $d-q$ frame

Figure 3.6: Synchronous speed reference frame transformation.

To apply this on the model, the well-known Park's transformation converts the abc electromagnetic quantities to $d-q$ ones. An example of this transformation , regarding voltage u_d and u_q, is calculated in (3.1), where θ is the angle from the electrical point of view, calculated in (3.2) and (3.3), for the stator and rotor respectively. Equally this transformation could be also applied for currents and magnetic flux. ω_m is the mechanical speed, ω_e the electrical speed and ω_{me} the mechanical speed from the fields point of view.

Please note that the homo-polar term was neglected because the machine is considered to be symmetric. For the synchronous machine, in steady-state, the mechanical speed will be equal to the synchronous one. Therefore, using the synchronous reference will be the same as using the rotor's reference.

$$\begin{bmatrix} u_d \\ u_q \end{bmatrix} = \frac{2}{3} \begin{bmatrix} \cos(\theta) & \cos(\theta - \frac{2\pi}{3}) & \cos(\theta + \frac{2\pi}{3}) \\ -\sin(\theta) & -\sin(\theta - \frac{2\pi}{3}) & -\sin(\theta + \frac{2\pi}{3}) \end{bmatrix} \begin{bmatrix} u_a \\ u_b \\ u_c \end{bmatrix} \tag{3.1}$$

$$\theta_s = \int \omega_e dt \qquad \omega_e = 2\pi f \tag{3.2}$$

$$\theta_r = \int (\omega_e - \omega_{me}) dt \qquad \omega_{me} = n_{pp_{rotor}} \omega_m \tag{3.3}$$

3.2.2 $d-q$ - Circuit

The equivalent electric circuit used is based on synchronous $d-q$ reference frame where magnetic saturation effects are included through an equivalent resistance and lumped parameters, such as $d-q$ inductance and iron core resistance, R_{Fe}, are estimated with results from static FEM. The synchronous $d-q$ reference frame for a steady-state IPMSM equivalent circuit is shown in Fig. 3.7.

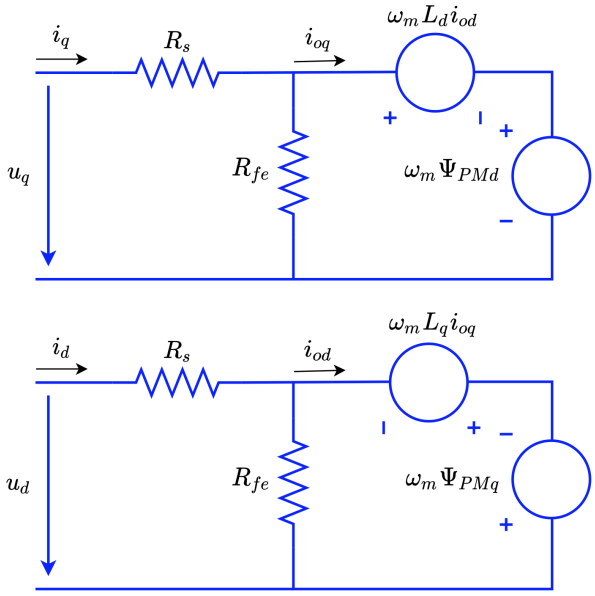

Figure 3.7: d and q axes steady-state model in the rotor flux reference frame. Adapted from [28].

The steady-state equations that describe the three-phase machine, according to the equivalent circuits, are given in (3.4) to (3.7), where u_d, u_q, i_d and i_q are the $d-q$ axes voltages and currents, and i_{od} and i_{oq} are the torque generating currents. The phase winding resistance R_s and the PM linked flux Ψ_{PM}, which for the considered machine topology is aligned with d-axis, represent the thermal variations since both are temperature dependent. The magnetic core effects are represented by the iron losses resistance, in the value of R_{Fe}, and the $d-q$ inductance's, L_d and L_q. ω_m is the rotor angular speed.

$$u_d = R_s i_d - \omega_m L_q i_{oq} - \cancel{\omega_m \Psi_{PM,q}} \tag{3.4}$$

$$u_q = R_s i_q + \cancel{\omega_m L_d i_{od}} + \omega_m \Psi_{PM,d} \tag{3.5}$$

$$\cancel{i_{od}} = i_d + \frac{\omega_m L_q i_{oq} + \cancel{\omega_m \Psi_{PM,q}}}{R_{fe}} \tag{3.6}$$

$$i_q = i_{oq} + \frac{\cancel{\omega_m L_d i_{od}} + \omega_m \Psi_{PM,d}}{R_{fe}} \tag{3.7}$$

To simplify the simulation of the electrical motor, a field-oriented control strategy was used, considering $i_{od} = 0$ and $\Psi_{PM,q} = 0$. This simplifies the machine's model equations and thus the calculation of the torque, T, decreasing the number of FEM simulations required and the computational time for the simulation, as the computation of L_d is not necessary anymore.

The steady-state torque, which has two components, the electromagnetic torque T_{EM} and reluctance torque T_{Rel} can be computed using (3.8), where n_{pp} are the number of pole pairs.

The electromagnetic component of the generated torque, T_{EM}, was chosen to be optimised as it gives a good indication of the total torque of the machine.

$$T = T_{EM} + \cancel{T_{Rel}} = \frac{3}{2} n_{pp} (\Psi_{PM,d} i_{oq} - \cancel{\Psi_{PM,q} i_{od}} + \cancel{(L_d - L_q) i_{od} i_{oq}}) \tag{3.8}$$

To these equations, the used parameters of $d-q$ inductance, L_d, was calculated using the FEM analysis.

3.2.3 Losses Calculation

This section targets the calculation of the losses in the EM's model. It is important to have a detailed study of this topic since it has a high impact on the motor efficiency and overall functioning.

The losses were divided in core losses, permanent magnet losses and copper losses. Few calculations were done using some estimations that are detailed below.

Core Losses

The estimation of magnetic core and PM's losses in IPMSMs is usually made by time-dependent FEM simulations for a certain rotation speed to consider the flux density harmonics in the core [29], however, a stationary approach was used here so that the model can have the lowest computational time possible, as it will be used in the optimisation algorithm.

To refine the obtained solutions, a more accurate loss model can be applied to selected elements of the optimisation's last generation, and therefore, for optimisation purposes, a rough estimation of iron losses is sufficient. Since traction application motors work at variable speed, the worst-case scenario is taken into account by considering the locked rotor method [30] for the estimation of the iron core losses, regarding only the magnetic flux fundamental component.

With these considerations, the iron losses are roughly estimated by an aggregate of three components: hysteresis losses, eddy current losses and excitation losses, obtained from loss curve data provided by the manufacturer, considering a sinusoidal variation of the flux density between the d and q axes, in the rotor and stator cores. Hysteresis losses take into consideration the B-H curve, eddy current

losses include the currents induced by the electromotive force generated in the stator core and excitation losses regards to the synchronous state of the EM.

Besides neglecting the effects of harmonics, the effects of minor loops and DC bias on hysteresis losses on the rotor core, are also ignored [31].

In (3.9) core loss density, p_{core}, is calculated with Steinmetz equation, where K_{hyst}, K_{eddy} and K_{exci} are the hysteresis, eddy current and excitation losses coefficients respectively and are obtained from loss curve data, considering sinusoidal variation of the flux density in the rotor and stator cores.

$$p_{core} = K_{hyst}B^2 f + K_{eddy}(Bf)^2 + K_{exci}(Bf)^{1.5} \tag{3.9}$$

Where B is the amplitude of magnetic flux density, obtained from FEM of the cases where stator flux is aligned with d and q rotor's axes, and f is the frequency of the flux density.

Equations (3.10) bear the constant values of the Steinmetz's coefficients for the material NO15.

$$K_{hyst} = 3.205 \times 10^{-5}[W/(fT^2kg)] \tag{3.10a}$$

$$K_{eddy} = 7.278 \times 10^{-5}[W/(f^2T^2kg)] \tag{3.10b}$$

$$K_{exci} = 1.09 \times 10^{-4}[W/(f^{1.5}T^{1.5}kg)] \tag{3.10c}$$

Equations (3.11) bear the constant values of the Steinmetz's coefficients for the material Vacoflux 50.

$$K_{hyst} = 2.453 \times 10^{-4}[W/(fT^2kg)] \tag{3.11a}$$

$$K_{eddy} = 9.0379 \times 10^{-6}[W/(f^2T^2kg)] \tag{3.11b}$$

$$K_{exci} = 8.854 \times 10^{-4}[W/(f^{1.5}T^{1.5}kg)] \tag{3.11c}$$

Consequently, since the losses coefficients are obtained per unit of mass, there is the need for integration the density losses along with the machine's magnetic core.

Permanent Magnets Losses

With the purpose of reducing eddy-current losses in the PMs, to improve the machine's performance and decrease the risk of demagnetisation, an analytical model to calculate the losses density in the PMs was applied [32]. Such model, calculated in (3.12), is a valid analytical approximation for parallelepiped shaped PMs while neglecting skin effect, as seen in Fig. 3.8 where L_{motor} is the motor's depth, l_m and w_m are the magnets length and width respectively and ρ_{PM} is the resistivity of the PMs (1.3×10^{-6}@120° C).

$$p_{PM} = \frac{\pi^2 f^2 B^2}{8\rho_{PM}} \frac{l_m^2 L_{motor}^2}{l_m^2 + L_{motor}} \tag{3.12}$$

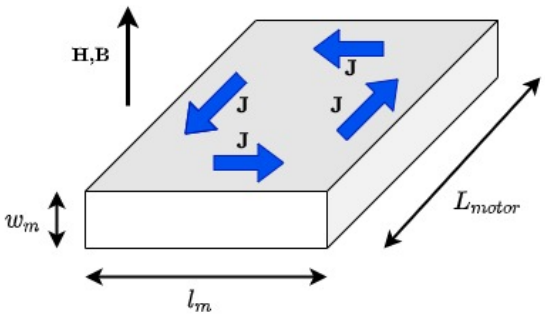

Figure 3.8: Cross-section of one pole magnet.

After the computation of the core and PM's losses density, these are used in (3.13) to calculate the equivalent iron losses resistance, R_{fe}. Where ρ_{core} and V_{core} are core's losses density and core's volume with and ρ_{PM} and V_{PM} the PM's losses density and PM's volume.

$$R_{fe} = \frac{3}{2} \frac{(\omega_m (L_d i_{od} + \Psi_{PM}))^2 + (\omega_m L_q i_{oq})^2}{\rho_{core} V_{core} + \rho_{PM} V_{PM}} \tag{3.13}$$

Copper Losses

The phase winding's resistance R_s can be estimated from (3.14), where N_{turns} is the number of turns, l_{cu} is the length of one loop, $A_{\varnothing}$ the wire section area and ρ_{cu} is the copper resistivity at temperature T. f_w is a filling factor, A_{slot} is the area of the slot available to the coil and N_{par} is the number of parallel wires.

$$R_s = N_{turns} \frac{l_{cu}}{A_{\varnothing} \rho_{cu}} = \frac{f_w A_{slot}}{N_{par}} \frac{l_{cu}}{\rho_{cu} (A_{\varnothing})^2} \tag{3.14}$$

The copper winding's losses are then obtained in (3.15), in function of the phase winding's resistance, R_s. Where i_d and i_q are the d and q axes currents and R_s the phase winding resistance.

$$P_{copper} = \frac{3}{2} R_s (i_d^2 + i_q^2) \tag{3.15}$$

3.2.4 Finite Element Model (FEM)

A FEM of the synchronous machine was developed to calculate the magnetic flux distribution and magnetic inductance originated for each geometry. Therefore, the use of optimisation tools has been allowing the improvement of EM's performance, the increase of their current power density and efficiency limits.

Periodic Conditions

In Fig. 3.9 the cross-section is presented just by one-quarter of the entire geometry, with each domain defined as it correspondent materials. From the machine's symmetry, it was possible to reduce the

simulation of the whole machine into one-quarter, simulating only one pole pair of the machine. This reduction was used during the project to perform all the computational calculations and optimisation process with reduced complexity and within a feasible computation time of the model.

A periodic continuity condition was applied to the internal boundaries, where the geometry was sliced along the flux density distribution, so the results would be the same as using the entire geometry.

In Fig. 3.9 the boundaries in question are represented in blue colour and respectively identified.

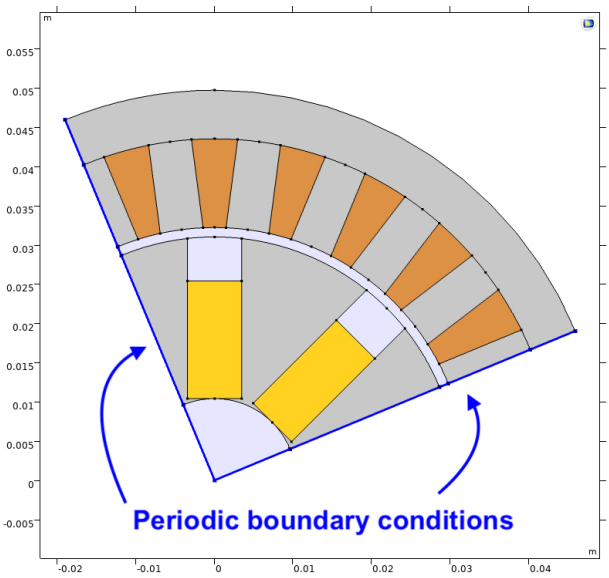

Figure 3.9: Cross-section of sliced geometry.

Maxwell's Equations

$$\nabla \times \mathbf{H} = \mathbf{J} \tag{3.16a}$$

$$\nabla \times \mathbf{E} = -\frac{\partial \mathbf{B}}{\partial t} \tag{3.16b}$$

$$\nabla \cdot \mathbf{B} = 0 \tag{3.16c}$$

$$\mathbf{J} = \sigma \cdot \mathbf{E} \tag{3.16d}$$

$$\mathbf{B} = f(\mathbf{H}) \tag{3.16e}$$

Mesh Configuration

For the validation of a FEM study, the mesh size and quality are crucial considering that there are multiple factors directly affecting the computation of the problem, including how long it takes the model to solve, the amount of memory required to compute the problem, how the solution is interpolated between nodes and the accuracy of the solution. Mesh refinement has a computational cost, therefore balance needs to be set between desired accuracy and the size of the computational grid, as low mesh resolution can lead to inaccurate results.

For the machine, the process of meshing the model geometry by having the software doing it automatically trough a physics-controlled mesh sequence type was decided. On the software used there were nine different predefined mesh sizes, *Extremely coarse* to *Extremely Fine*, and their convergence analysis was taken into consideration. In Fig. 3.10 is presented a graph of the magnetic flux density, for each different mesh size, on a singular point set in the middle of one stator tooth, in a place, where it is not influenced by the mesh size, and distant from singularities that can also disturb the final result. With these convergence results, the predefined meshes that are more suitable, can be observed.

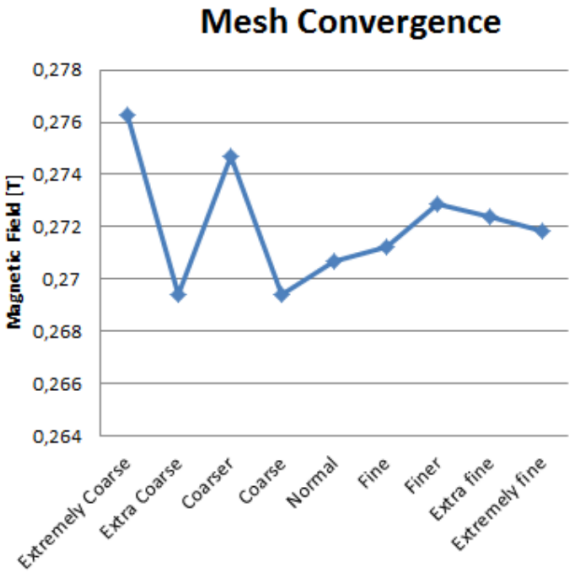

Figure 3.10: Default FE software mesh convergence analysis [27].

Additional data is presented in table 3.6 where it can be observed that the study time is feasible from *Extremely Coarse* to *Fine* meshes. From *Finer* to *Extremely Fine* the time increases substantially. Furthermore, this time does not include the time to build the mesh which, for *Extra* and *Extremely Fine* meshes is significant. The average quality is a control parameter available from the FEM analysis software that rates the mesh elements from 0 to 1, being 0 a degenerated/deformed element and 1 a perfectly regular element.

Element Size	Domain Elements	Average Quality	Computational Time [s]
Extremely Coarse	8934	0.6390	12
Extra Coarse	20766	0.7027	18
Coarser	32548	0.2932	32
Coarse	41670	0.7783	35
Normal	81768	0.7554	77
Fine	85982	0.7994	83
Finer	219724	0.8169	224
Extra Fine	349952	0.8258	332
Extremely Fine	1192362	0.8436	1381 (23 min)

Table 3.6: Different default meshes parameters. Adapted from [27].

Regarding this study in order to choose the best-suited mesh configuration for the machine, a different structured mesh on certain parts of the geometry was adopted. *Finer* mesh size was selected for the stator core, the PMs, the air gap and the rotor slot domains with a maximum element size of $0.00242m$ while a *Coarse* size was elected for the rotor core and shaft domains with a maximum element size of $0.00653m$. This was done to reduce time and memory requirements, thereby creating an efficient and accurate simulation.

This elected mesh configuration is shown in Fig. 3.11.

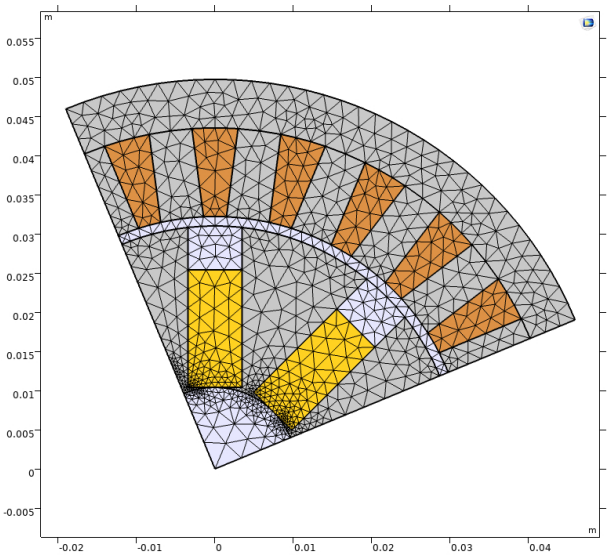

Figure 3.11: Elected mesh configuration.

Coil Flux Calculation

From the analysis of a generic topology of the IPMSM, and for the considered number of poles and stator slots, the direct and quadrature axes, $d-q$, are $\theta_{me} = 0°$ and $\theta_{me} = 22.5°$, respectively. This can be seen in Fig. 3.12 in blue colour.

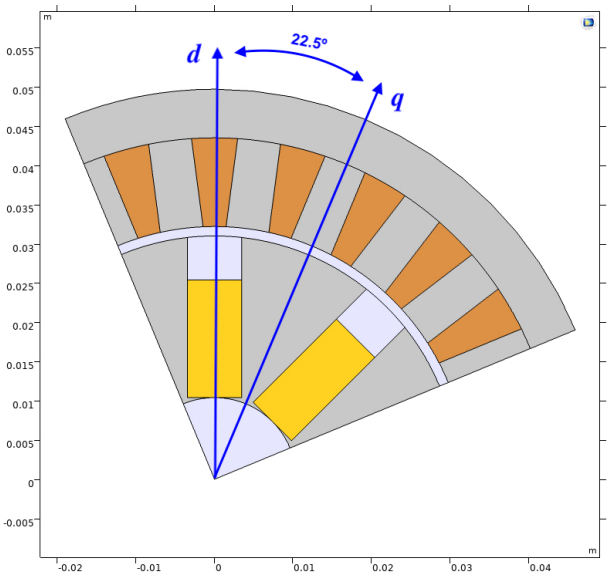

Figure 3.12: Representation of rotor's d and q axes.

A stationary-time simulation for the $d-q$ axes is considered and the current in each phase is given by (3.17).

$$i_A = I_m cos(\omega t) \tag{3.17a}$$

$$i_B = I_m cos(\omega t - 2\pi/3) \tag{3.17b}$$

$$i_C = I_m cos(\omega t + 2\pi/3) \tag{3.17c}$$

Depending if the rotor's q and d axes are aligned with phase A, the Park transformation results in $i_{od} = 0$ and $i_{oq} = I_m$ or $i_{od} = I_m$ and i_{oq} =0, respectively.

To calculate the magnetic flux on both direct and quadrature axes, adjusting the rotor's position with the d and q axes, two calculations were made, to estimate from the FEM simulations the $d-q$ linked fluxes, Ψ_d and Ψ_q, and the flux density distributions, B_d and B_q.

First, the rotor was considered without the PM's flux (Br =0) and the stator current density was imposed, from zero to a maximum value defined by the optimisation tool, to calculate the winding's linkage flux in both axis, d and q. This allows the calculation of the L_d and L_q parameters.

The second calculation was made considering the rotor PMs (B_r =1.2 T) with zero induced current density ($J = 0$) with the PM flux aligned with the d-axis, to allow the calculation of the PM's d-axis linkage flux, $\Psi_{PM,d}$.

The estimation of R_{fe} in (3.13) from the locked rotor core losses method depends on the amplitude of the flux density B_m in the PMs, rotor and stator, calculated in (3.18). B_d and B_q are obtained by simulations with the stator flux aligned with d and q rotor axes and with $\Psi_{PM} \neq 0$.

$$B_m = |B_d - B_q| \tag{3.18}$$

Inductance Calculation

L_d and L_q inductances are computed from results of linked flux acquired, following the previous procedure, using the FEM. With PMs flux Ψ_{PM} reduced to zero (Ψ_{PM} =0), the stator is aligned with the rotor's d and q axes in positions of maximum and minimum flux linkage, respectively. Ψ_d and Ψ_q are acquired in function of i_d and i_q currents and for simplification, saturation is neglected. L_d and L_q inductances are determined in (3.19).

$$L_d = \left.\frac{\Psi_d}{i_{od}}\right|_{i_{oq}=0} \qquad L_q = \left.\frac{\Psi_q}{i_{oq}}\right|_{i_{od}=0} \tag{3.19}$$

Magnetic Flux Distribution

To avoid magnetic saturation and to limit the operation temperature of the materials, the following limits are imposed:

- $B_{Sat}(FeSi) =$ 1.6 T — Maximum flux density for FeSi
- $B_{Sat}(VCoFe) =$ 2.2 T — Maximum flux density for VCoFe
- $T_{amb} =$ 30° C — Room temperature
- $T_s =$ 120° C — Maximum surface temperature

To obtain an image of the magnetic flux distribution along with the machine, several strategic segments of the magnetic core are analysed using FEM analysis.

Two *Line Maximum* operations were done to calculate the magnetic flux density norm on the stator. One on a line crossing the stator teeth starting in the $d-axis$ phase coil pitch, where the flux is maximum and another circle line along the midpoint of the stator outer ring. These lines are presented in Fig. 3.13 in blue colour.

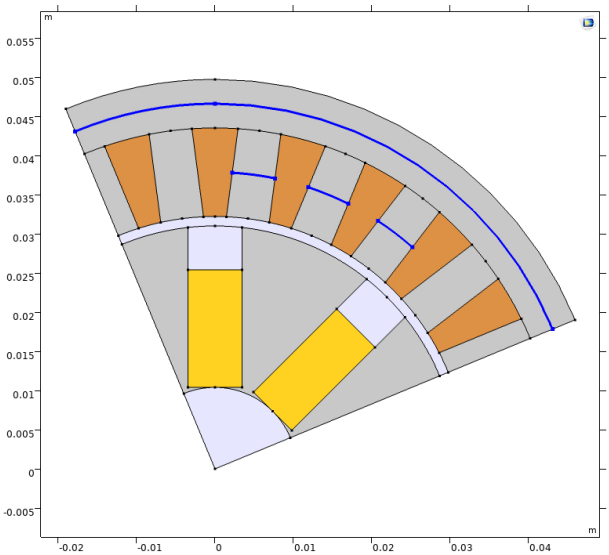

Figure 3.13: Magnetic flux density norm calculation in the stator.

Two *Surface Average* operations were done to calculate the magnetic flux density norm on the rotor. One surface is the core of the rotor and the other the PMs, as the non-uniform distribution on those domains makes it difficult to be characterised by a line. These surfaces are respectively presented in Fig. 3.14(a) and Fig. 3.14(b) in blue colour.

If the maximum flux density in these chosen segments on the stator or the average flux density rotor and PMs values are above a certain threshold, the core is considered to violate the magnetic constraint. This method is used to avoid localised peaks of high flux concentration resulting in the rejection of promising geometries during the optimisation.

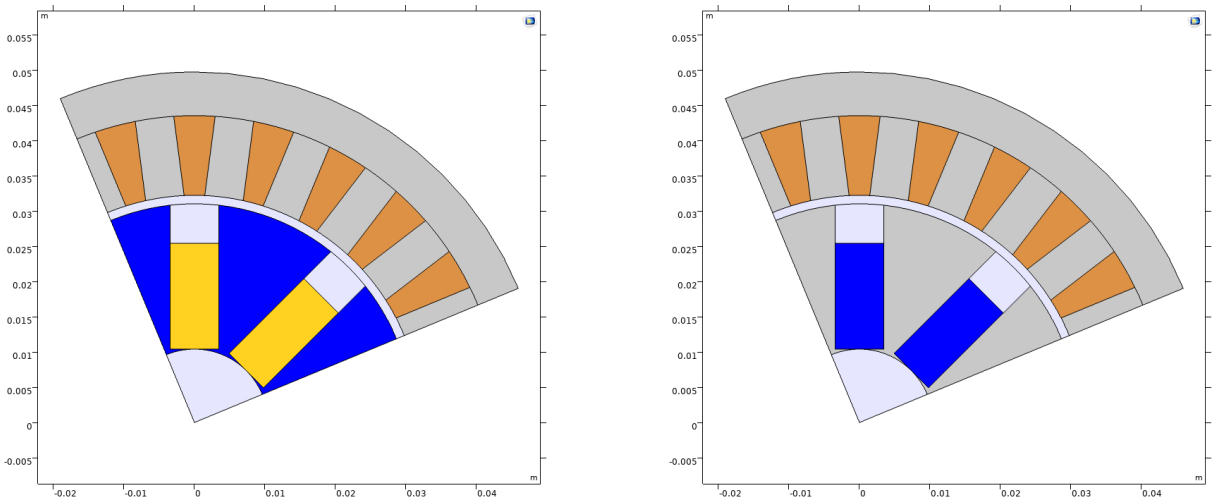

(a) Rotor core surface

(b) Permanent magnets surface

Figure 3.14: Magnetic flux density norm calculation in the rotor.

3.3 Thermal Model

The thermal behaviour has a high influence in the motor design and becomes critical to determine if a design is viable or not, since each material has a maximum withstanding temperature and the material's operating temperature will be imposed by the motor's losses. Therefore, it is important to have a thermal model capable of predicting the machine's operating temperature for a set of electric variables, such as current, frequency and magnetic flux. This thermal model will enable the discard of designs which overpass thermal limits as well as assess safety thermal margins of each optimised solution.

A simplified thermal model is considered to estimate the maximum operating point of the machine, with a single heat transfer coefficient representing the heat dissipation from the machine to the cooling system. The thermal model will be integrated in the model's optimisation so it must be computationally fast and sufficiently accurate. Thermal conduction in the rotor and stator core are neglected as the conductive thermal resistance in metallic materials is very low when compared to the convective ones.

Considering that the motor will be required to provide nominal power in short bursts, the maximum operating steady state temperature can be estimated for the worst-case scenario to evaluate if the optimisations are viable.

The opted cooling system will be water cooled by a previously design system [33]. This cooling system achieves a heat transfer coefficient of h =1000 Wm^{-2}k^{-1} and can be observed in Figure 3.15. Typical heat transfer coefficient values, for liquid-cooled forced convention, go from 50 to 20000 Wm^{-2}k^{-1} [34]. The estimation considers convective heat transfer in the air-gap and dissipation from the machine's surface to the cooling system environment.

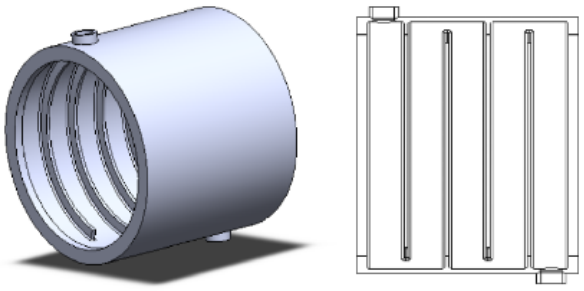

Figure 3.15: Motor sleeve with chicane piping layout [33].

The machine is considered as a cylinder that produces heat resulting from Joule losses in the rotor core, (3.9) and PMs, (3.12), which is dissipated through the air-gap and, together with the stator and copper winding's losses, (3.15), trough the cooling jacket and into the environment.

The heat transfer is described by the thermal equation (3.20) where T_s and T_{amb} are the surface and ambient temperatures, h is the transfer coefficient, S is the machine's surface area and P_{core}, P_{PM}, P_{copper} are the magnetic core, PMs and copper losses, respectively.

$$(T_s - T_{amb}) = \frac{1}{hS}(P_{core} + P_{PM} + P_{copper}) \tag{3.20}$$

Chapter 4

Multi-Objective Optimisation

With the purpose of studying the Electrical Machine (EM) described in chapter 3 and how could it benefit from using VCoFe alloy as material core, an optimisation was done. The geometry described in section 3.1.1 is here optimised and the results from using VCoFe and FeSi are compared.

Due to the high number of variables and constraints, an optimisation algorithm was used and described in this chapter to obtain the highest torque and efficiency values.

The design optimisation, where the machine is subjected to the available space in the car is also detailed here with its objective functions, decision variables and thermal safety constraints being identified.

Contents

4.1 Genetic Algorithm

For EMs, multi-objective optimisation is important from the point of view of practical problem-solving. Instead of a single optimal solution, it provides a set of optimal solutions for the design of the machine. This multi-objective optimisation is coupled with a FEM and analytical expressions, due to the multiphysics involved, which are interdependent with non-linear materials. In this project, a genetic algorithm was opted since it is easy to understand, is one of the most reliable algorithms and the output can improve over time.

Non-dominated Sorting Genetic Algorithm II (NSGA-II) [11] was the chosen genetic algorithm since it has a fast non dominated sorting approach with $O(MN^2)$ computational complexity, is able to find a better spread of solutions and better convergence near the Pareto-optimal front, represented as P_t on figure 4.1. This algorithm allows the optimisation of various objective functions, with several constraints, using a fast and elitist approach where the best solutions of each generation are preserved to be optimised on the next generation and a diversity preserving mechanism is used, improving the diversity among solutions of the same non-dominated front.

4.1.1 NSGA-II Algorithm

With the decision variables the program generates N number of individuals, designed as population size, called Pareto front, P_t on figure 4.1. The next step is generating N number of individuals using selection, crossover and mutation from the P_t individuals, designed as parents, creating a new population Q_t, designed as children. Creating this new Q_t population, from the individuals of P_t, requires three different steps described below. They are repeated until the population Q_t has the same size as the parent population P_t. Adding these two populations a new R_t population of size $2N$ is created.

Tournament Selection

Tournament selection compares two parents chosen randomly out of the parent population P_t. First, these two individuals are compared by rank and after by crowding distance. The one with a better rank can reproduce. This is done twice, one time for parent number one and another time for parent number two. Every time there is a new random sampling for two persons and on this base, the parents and the DNA are known and cross over process can take place.

Crossover

Crossover simply takes the DNA of the chosen individuals and mixes them. It takes randomly half of the genes of one individual and changes them with the ones of the other one, creating two new individuals. These are called child number one and child number two.

Mutation

A mutation is randomly changing one of the child genes for a random value. Before adding the children to the Q_t population and starting the iterative process again, random mutations can occur. These mutations can be applied very individually. A random gene is picked and modified.

This process can be done until a certain number of children created equals the number of parents or until a convergence of the results. In this case, a specified number of individuals was the chosen option.

Once this is done, all individuals are ranked and sorted with the following different sorting steps. These steps are detailed below and the procedure scheme can be seen in figure 4.1.

Non dominated sorting - First sorting step

These sorting will separate all individuals into different groups. First, it tests all individuals of R_t population regarding constraints. The ones that fail these tests are automatically rejected. The ones that are accepted by all tests are then separated into different groups. The groups from $F1$ to Fn as seen on 4.1 will be made regarding the score of each individual. For this the algorithm gathers a certain number of neighbour individuals and regarding the scores will compare them and the ones with the better score will go to the best score group F1 and so on and on until every individual is compared with their neighbours and enclosed on the respective score group.

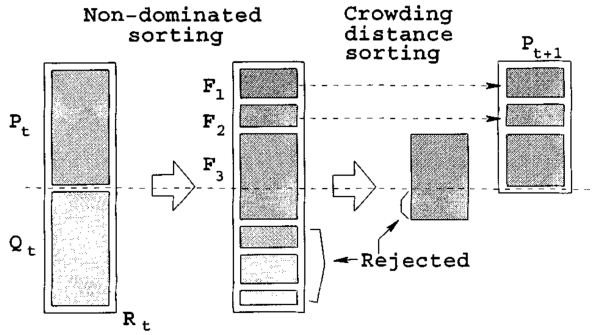

Figure 4.1: NSGA-II procedure [11].

Crowding distance sorting - Second sorting step

After the non-dominated sorting, a group of several different groups is sorted. These groups altogether have the double of individuals as our aim is. It is necessary to start rejecting some of the groups however, before taking the best fronts to the next generation, there is the need to bear in mind that probably at the time to reject the worst half of the individuals, one of the groups will be divided into rejected and not rejected individuals. To do this selection a crowding distance sorting was used.

To keep a good spread and to avoid local maximum-minimum, instead of finding the global ones, the crowding distance factor decides which individuals are added to the new population. The individuals with higher crowding distance are picked first. This means that individuals that are more isolated on the objective function space are elected.

The total crowding distance for each individual is represented in Fig. 4.2 and is calculated by (4.1) where n is the number of objectives.

$$distance(i) = distance(i) + \frac{(i+1).n - (i-1).n}{f_n^{max} - f_n^{min}} \tag{4.1}$$

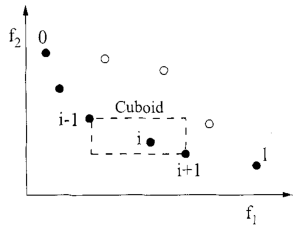

Figure 4.2: Crowding distance calculation [11].

4.2 Design Optimisation

The design optimisation targets the best possible geometry design for the studied IPMSM, using multiple decision variables in order to have the best objective function's results. The goal is to maximise electromagnetic torque and efficiency without reaching any constraints of geometrical boundaries, inverter's limit or thermal safety.

The cooperation between FEM and analytical models enables an adequate accuracy for a much faster estimation of the machine's overall performance. In Fig. 4.3, the combination of these models is shown. This theoretical simulation study provides preliminary outcomes on the practical use of IPMSM using VCoFe as core material.

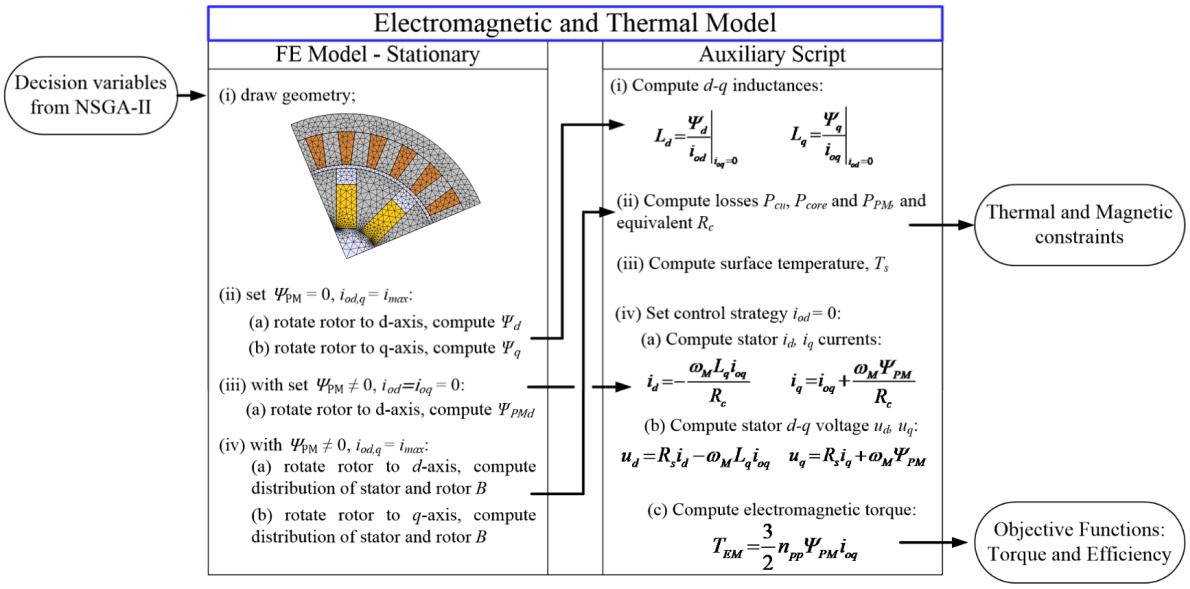

Figure 4.3: Combination between FEM and analytical models.

Both FeSi and VCoFe alloys are used in the optimisation. The best overall performance of each machine is reached for either material and compared using the respective final Pareto front, for a frequency

of 400 Hz. This frequency was set due to requirements of the FST competition.

4.2.1 Objective Functions

Since the aim is to compare FeSi and VCoFe as material core for the spoke-type IPMSM FST's car, the objective is to reach the electromagnetic torque maximisation, T_{EM}, and, since this one is limited by the decision variables and the constraints, it is directly related with the efficiency maximisation, η, resulting in a multi-objective optimisation and therefore the results are presented by a 2D curve of T_{EM} vs η.

A characteristic of genetic algorithms is that all objective functions are to be minimised given that NSGA-II is resilient to local optimal points, making it suitable for finding the global minimum of the solution space, populating it evenly, which is relevant for the intended comparative analysis. Consequently, the objective function was used to minimise the negative value of T_{EM} and η without the saturation of the magnetic core or exceeding the material's withstanding temperature. As such, the objective functions are:

$$f_{1,2}(x) = \begin{cases} \min(-T_{EM}) \\ \min(-\eta) \end{cases} \equiv \begin{cases} \max(T_{EM}) \\ \max(\eta) \end{cases} \tag{4.2}$$

To reduce the computational time, a simplification of the machine's model equations was done, using the electromagnetic component of the generated torque as a good indication of the total torque of the machine, calculated in (4.3).

$$f_1(x) = T_{EM} = \frac{3}{2} n_{pp} \Psi_{PM} i_{oq} \tag{4.3}$$

The objective function concerning the efficiency is calculated in (4.4).

$$f_2(x) = \eta = \frac{T_{EM}\omega_M}{T_{EM}\omega_M + \rho_{core}V_{core} + \rho_{PM}V_{PM}} \tag{4.4}$$

4.2.2 Decision Variables

The DNA of each individual is an optimisation vector, with nine different variables, that generates values for the objective functions. These specific variables called decision variables, or genes, are independent variables that are going to be changed to obtain optimal solutions, defining a unique 2D model design. Following the study being a multi-objective optimisation, the candidate solution form the Pareto front of the objective functions $f_1(x)$ and $f_2(x)$ in (4.2) , where an improvement for $f_1(x)$ can be a downgrade to $f_2(x)$ or vice-versa. This solution provides a pair of results for T_{EM} and η, being unique for each optimisation vector.

These decision variables are the torque producing current density of the $q-axis$, J, and the geometry dimensions of the rotor radius, shaft radius, magnet width, magnet length, teeth width, teeth length, outer stator width and air-gap size. Resulting in an optimisation vector, $\boldsymbol{x}$, of nine decision variables.

$\boldsymbol{x} = [J, r_r, r_s, w_m, l_m, w_t, l_t, w_s, g]$

To reach feasible solution geometries, lower and upper boundaries must be imposed to real and pretended boundaries for the motor in question. The boundary's limits for dimensions in Fig. 4.4 are presented in the table of Fig. 4.1. The current density, J, was set between 1 and 40 A/mm^2, regarding temperature constraints.

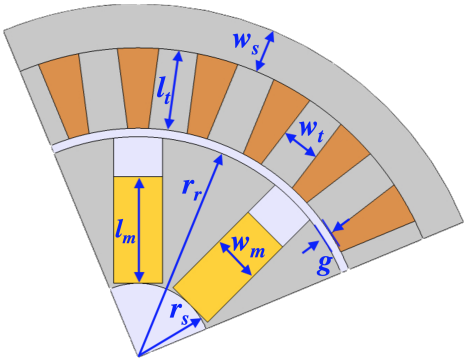

Figure 4.4: Geometry dimensions.

Variable	Description	Boundaries
J	Current density	1-40 [MA/m^2]
r_r	Rotor radius	20-40 [mm]
r_s	Shaft radius	5-30 [mm]
w_m	Magnet width	1-15 [mm]
l_m	Magnet length	5-20 [mm]
w_t	Tooth width	1-10 [mm]
l_t	Tooth length	7-20 [mm]
w_s	Outer stator width	1-20 [mm]
g	Air-gap	1-1.5 [mm]

Table 4.1: Geometry dimension's boundaries.

After assigning the dimension's boundaries was time to build the machine with FEM tool. Some dimensions made the machine physically impossible to build, these incompatibilities were gathered and used as geometrical constraints.

4.2.3 Constraints

Not only the dimension's boundaries had to be taken into account but also the manufacturing feasibility of the motor, with the optimised geometry. In table 4.2, the constraints considered regarding geometrical dimensions and weight are presented, as well as inverter's, thermal and magnetic limits.

The geometrical constraints are simply imposed by the user according to application-specific requirements, such as maximum dimensions and weight, whereas thermal limitations and magnetic constraints are reliant on the magnetic saturation of the chosen core material, leading to less efficient geometries, and temperature safety, protecting PMs and winding isolation. The inverter's constraint is merely its limit of operation.

	Design constraints	Constraint values
Geometrical	Weight	5 kg
	Outer radius of the motor	50 mm
	Stack length of the motor	80 mm
Inverter	Peak currrent	100 A
Thermal	Copper winding's temperature	180° C
	Permanent magnet's temperature	120° C
Magnetic	Magnetic flux density for FeSi	$<$1.6 T
	Magnetic flux density for VCoFe	$<$2.2 T

Table 4.2: Design constraints.

After defining the depth of the motor, L_{motor}, to 80 mm and the motor's outer radius, R_{motor} to 50 mm, a program script was created to build as many random geometries as desired, without violating any of the constraints. Objective functions and constraints are evaluated with presented electromagnetic and thermal models for each generation.

The dimensions were distinct with a discrete step of 0.1 mm, in order to decrease the entire population space to have a lower computational time and given that higher manufacturing tolerances are harder to reach.

Meanwhile, after the first optimised geometries were created, a set of dimension constraints got the need to be added in the interest of excluding non-physically possible machine creations. These are the following:

- The slot between the PM and the air-gap had to be at least 1 mm.
- The minimum distance between two teeth had to be more or equal to 1mm.
- The minimum distance between two PMs had to be more or equal to 1mm.

Chapter 5

Results

The optimisation results of the designed IPMSM are provided in here.

A pre-study was done on where the motor should function regarding magnetic flux density to obtain the preferred working area.

The final optimisation results are afterwards presented, both for VCoFe and FeSi, and described for the optimised last generation of the NSGA-II algorithm.

To understand an unpredictable result among the optimisation results, an air-gap length study and simulation was performed.

Contents

5.1 Preferred Working Area

EMs designed for traction applications require high-performance ratios. This performance is reached when EM working area is just below saturation. The border between the saturation region and the preferred working area is commonly named as knee point. It is represented in the B-H magnetisation curve of Fig. 5.1, in blue, as well as the different regions of EM work.

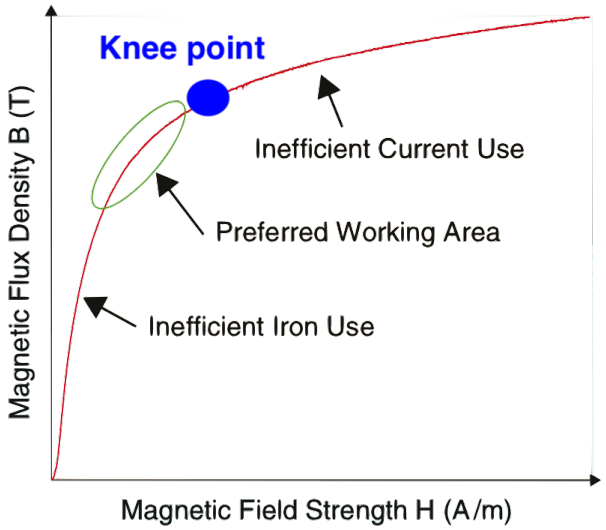

Figure 5.1: Machine operating areas of the material's B-H curve. Updated from [2].

As the magnetic flux increase in the linear region of the B-H curve, generated electromotive force rises until the magnetic saturation is reached. Although operating closer to the knee point results in increased core flux density, the risk of voltage over passing the knee point and reaching the saturated region is high. Consequently, working in an inn-efficient current zone, where magnetising inductances values become low and a small rise in flux demands a large rise in field current, is not recommended.

With the indecision on where to have the model design operating, whether aiming for a riskier but more efficient region or a safer but less efficient region, a study was carried out where three machines were optimised with different constraints regarding the maximum magnetic flux density.

In Fig. 5.3 can be seen the different constraints being met for the three studied optimised model designs, where the maximum magnetic flux density for each machine design, presented in Table 5.1, were chosen regarding the B-H magnetisation curve of each used material in Fig. 5.2. With blue blue colour corresponding to FeSi and red colour to VCoFe.

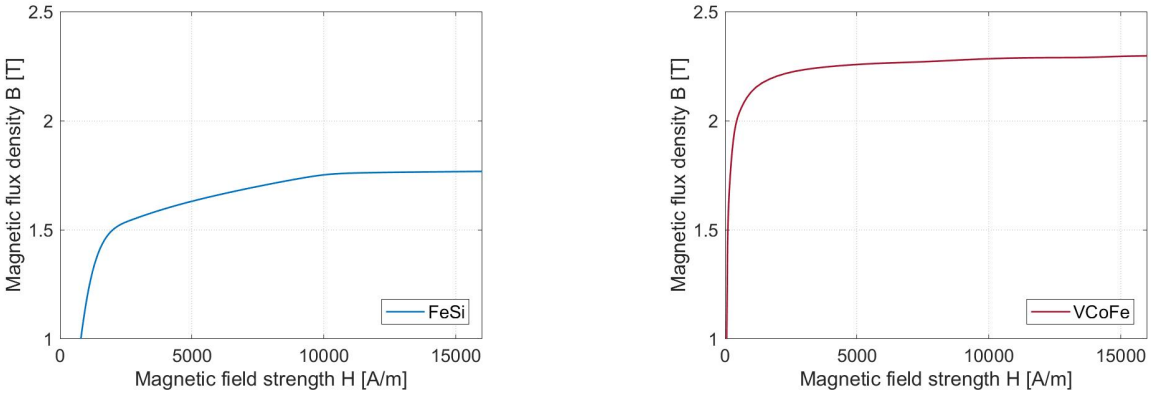

(a) FeSi, NO15

(b) VCoFe, Vacoflux 50

Figure 5.2: B-H magnetisation curves of the FeSi and VCoFe materials used.

	Design A	**Design B**	**Design C**
FeSi	<1.5 T	<1.6 T	<1.7 T
VCoFe	<2.1 T	<2.2 T	<2.3 T

Table 5.1: Maximum magnetic flux density for each design studied.

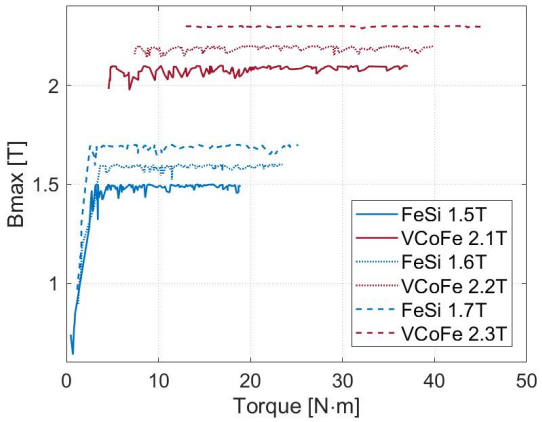

Figure 5.3: Maximum magnetic flux density for the three different machine designs.

The Pareto front obtained from the optimisation of the three different design models is in Fig. 5.4. A clear relation between the torque and the magnetic flux constraint can be observed. Where an increase in the maximum allowed magnetic flux generates higher efficiency.

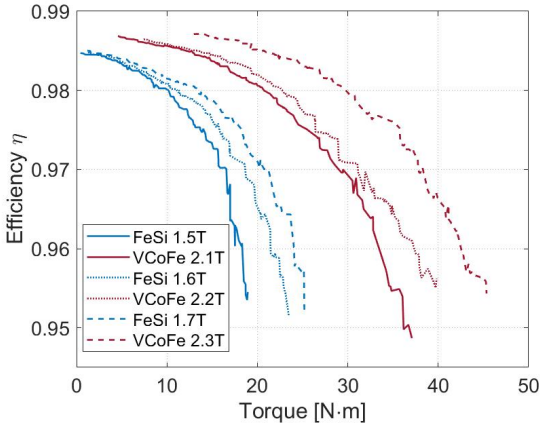

Figure 5.4: Pareto front of the three different machine designs.

In Fig. 5.5 the linked magnetic flux in the PMs regarding the direct axis, $\Psi_{PM,d}$, is observed for the three different designs. Contrarily to the efficiency, the linked magnetic flux does not represent a noteworthy improvement with the increase of the maximum magnetic flux.

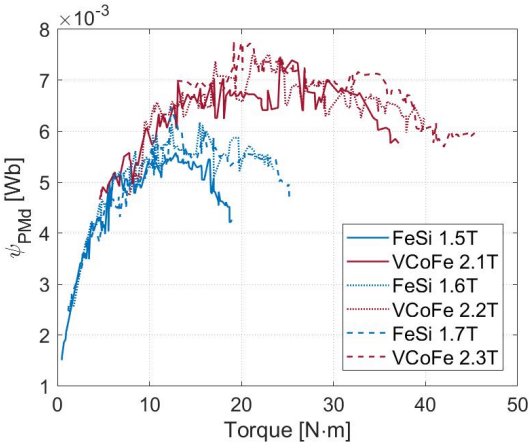

Figure 5.5: Linked flux in the PMs with $d-axis$ orientation for the three different machine designs.

Regarding this results, the maximum magnetic flux constraint elected for the optimisation of the model design machine was $<$1.6 T and $<$2.2 T, for FeSi and VCoFe respectively. With the objective of reaching a remarkable torque and efficiency value with a lower risk of magnetisation.

5.2 Optimisation Results

The optimisation was done regarding both FeSi and VCoFe materials separately, using a genetic NSGA-II with a population of 200 elements and 150 generations for each optimisation, defined empirically based on a set of previous tests with a feasible time for convergence, as FeSi optimisation takes around 26 hours and VCoFe optimisation around 30 hours. For each optimisation, the solutions were arranged increasingly by its torque.

The final Pareto front obtained for the maximisation of the torque and efficiency, from the last generation, is presented in Fig. 5.6, with every solution meeting all the constraints previously described in the constraints section, 4.2.3. An efficiency decrease can be observed with the increase of the torque and values of 98.2% with VCoFe and 96.5% with FeSi materials are reached for a 20 Nm torque machine required by FST. Where VCoFe outperforms FeSi in an estimated increase of up to 3% in efficiency for the same torque, or up to 70% torque increase for the same efficiency level. For the FST competition car, with a required 20 Nm of nominal torque, there is an efficiency increase of 1.7%.

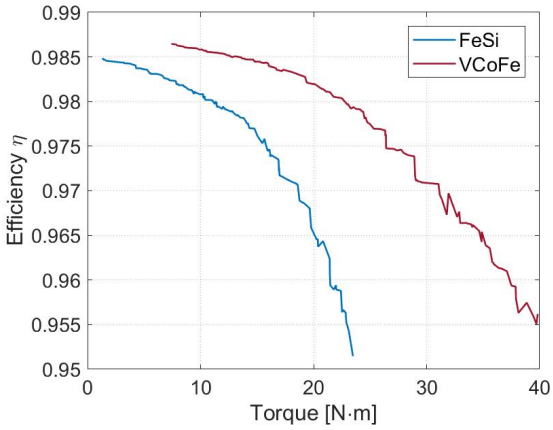

Figure 5.6: Pareto front of the last population optimisation.

Is shown in figures 5.7(a) and 5.7(b) the magnetic and thermal constraints being met, with J_{th} corresponding to the maximum current allowed, limited by the thermal constraints. Considering that the cooling system is well-dimensioned, thermal constraints do not limit the machine's performance. However, as the magnetic flux density on both solution is at the maximum value, 1.6 T and 2.2 T for FeSi and VCoFe respectively, the magnetic constraint is the limiting factor.

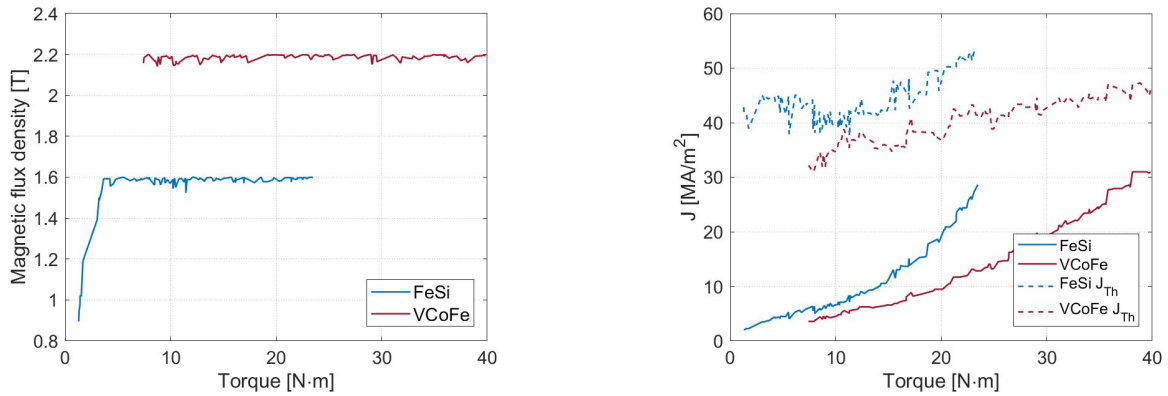

(a) Magnetic flux density (b) Thermal current density

Figure 5.7: Magnetic and thermal constraints.

In Fig. 5.8 the core and copper losses of the machine, for both FeSi in blue and VCoFe in red, are presented. Analysing these graphs, is possible to identify in Fig. 5.8(a) the same approximate losses in both machine cores, with slight inferior results for the FeSi machine. Regarding winding copper losses, it is clear in Fig. 5.8(b) that VCoFe outperforms FeSi with remarkable reduced losses. These calculations of the machine losses are described in the losses calculation section, 3.2.3.

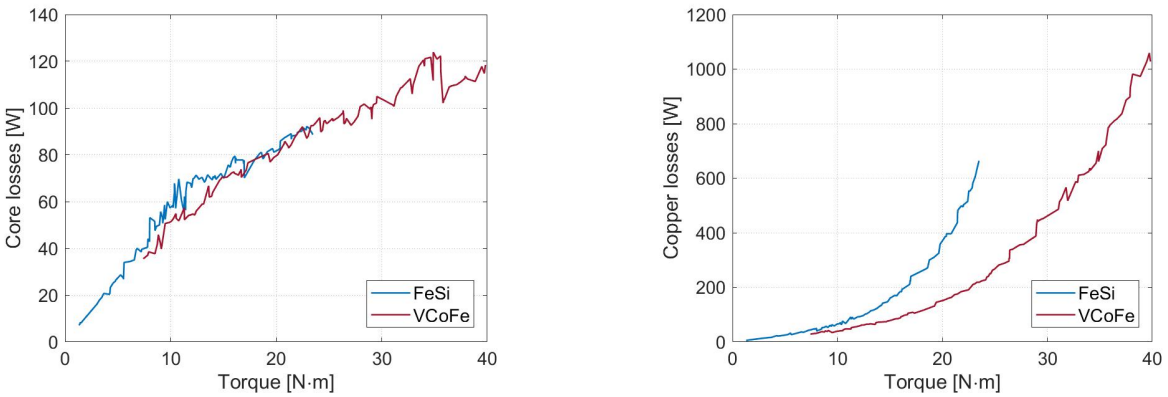

(a) Core losses (b) Copper losses

Figure 5.8: Core and copper losses.

Reaching high current densities to maximise torque, outcomes in dimensions modifications with the purpose of keeping the magnetic flux density around constraint level, resulting in a decrease of efficiency and an increase of the core volume. This can be seen in Fig. 5.9(a), where, for the same torque value, the core volume of the VCoFe machine is around 10% smaller than the machine of the FeSi optimisation. For the FST competition car, with a required 20 Nm of nominal torque, there is a reduction of 11% in core volume for the motor.

Nevertheless, due to the material density being higher for the VCoFe alloy, 8120 kg/m^3, than FeSi alloy density, 7650 kg/m^3, this difference is not noticeable in core weight, Fig. 5.9(b).

In respect of this, torque density for both core materials is similar for similar torque regions, however, since it is possible to achieve higher torque densities with higher nominal torque with VCoFe material,

these machines present increased torque with similar weights, compared to FeSi machines from lower torque ranges.

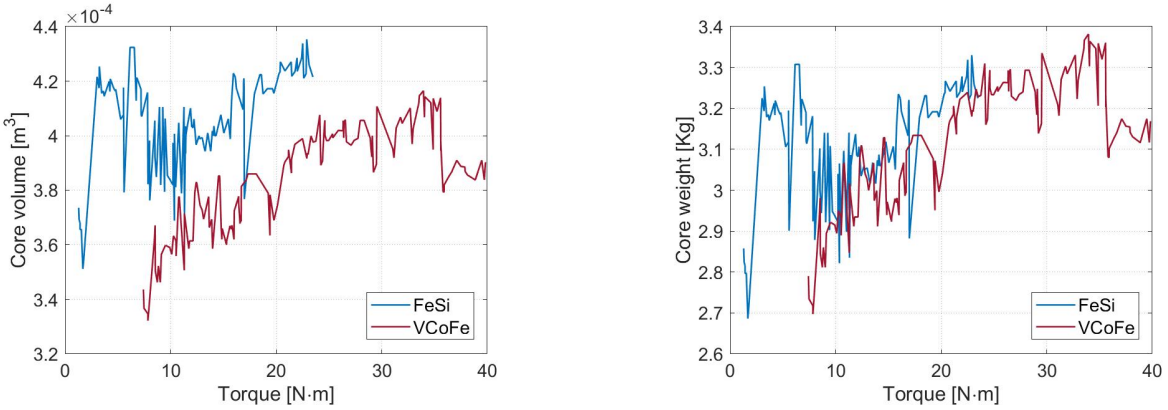

(a) Core volume (b) Core weight

Figure 5.9: Volume and weight of the machine optimisation.

Current density and the dimensions of the machine, are presented in figures 5.10 and 5.12, being these the optimised decision variables.

In Fig. 5.10 can be noted that the torque increases with current density, J, for both materials. PMs dimensions, in figures 5.12(c) and 5.12(d), are at the maximum possible for each geometry to maximise linked flux and torque. VCoFe achieves higher magnet widths, consequently resulting in more magnetic flux.

A study of the air-gap length from Fig. 5.12(g) and the reason why it does not always have the minimal length is demonstrated below in the air-gap length study section, 5.3.

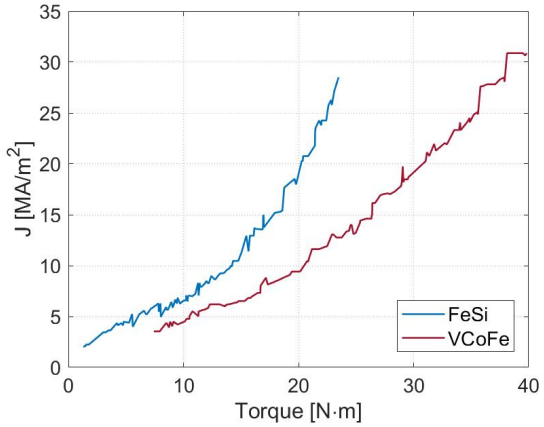

Figure 5.10: Current density.

In Fig. 5.11 a final optimised solution for the machine reaching $T = 20$ Nm, as required for the FST, is presented both for FeSi and VCoFe. Where the coloured bars represent the magnetic saturation. The final optimised dimensions for this solutions can be seen in table 5.2.

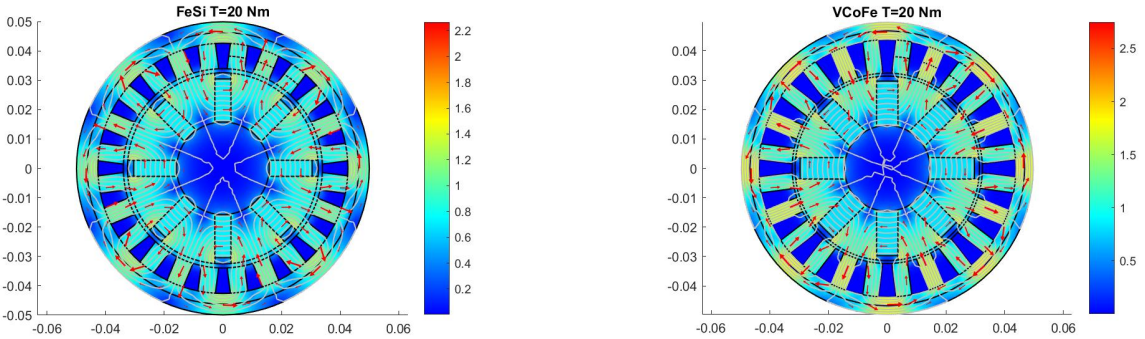

(a) FeSi simultation

(b) VCoFe simulation

Figure 5.11: Optimised solution for $T = 20$ Nm.

Variables	Description	FeSi	VCoFe
J	Current density	17.98	9.41 [MA/m^2]
r_r	Rotor radius	32.6	31.4 [mm]
r_s	Shaft radius	15.8	14.6 [mm]
w_m	Magnet width	05.5	07.3 [mm]
l_m	Magnet length	14.7	15.1 [mm]
w_t	Tooth width	06.0	05.3 [mm]
l_t	Tooth length	08.7	11.4 [mm]
w_s	Outer stator width	07.3	05.9 [mm]
g	Air-gap	01.4	01.0 [mm]

Table 5.2: Optimised geometry dimensions for $T = 20$ Nm.

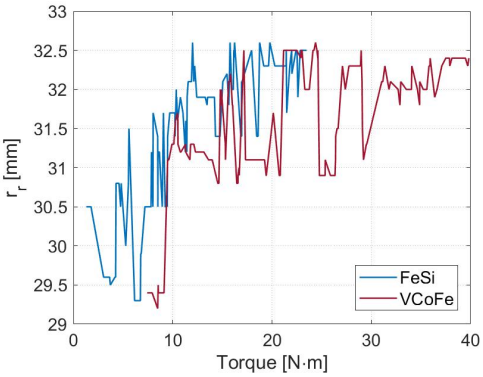

(a) Rotor radius, r_r

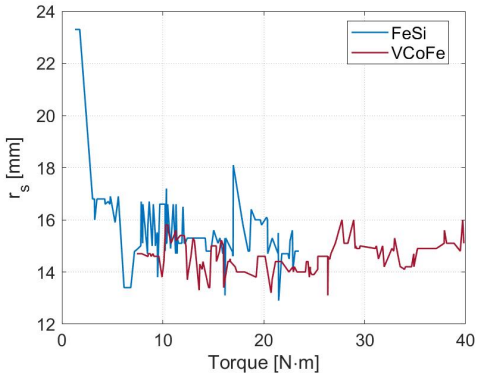

(b) Shaft radius, r_s

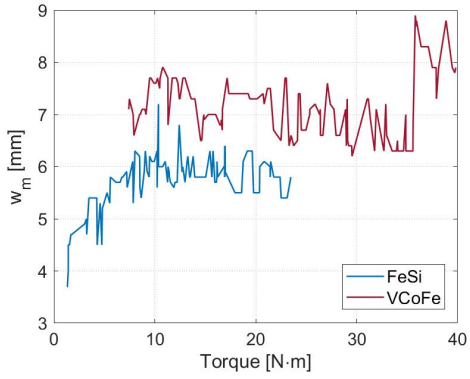

(c) Magnet width, w_m

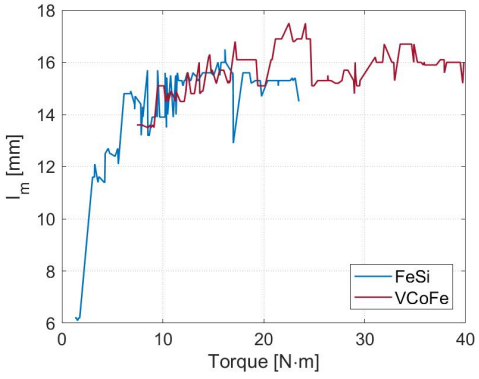

(d) Magnet length, l_m

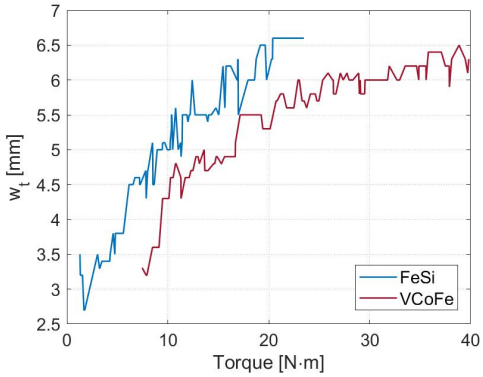

(e) Teeth width, w_t

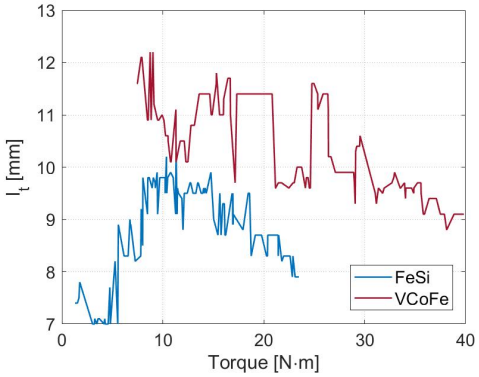

(f) Teeth length, l_t

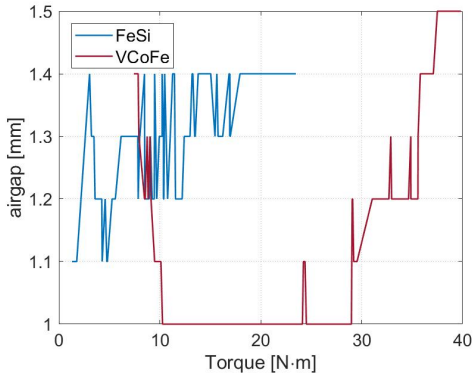

(g) Air-gap length, gap

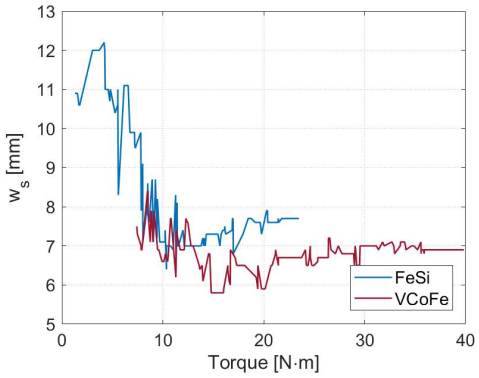

(h) Stator outer ring width, w_s

Figure 5.12: Dimensions optimisation.

5.3 Air-gap Length

The distance between the outer surface of the rotor and the inner surface of the stator, where an actual physical gap separates these two parts, is named the air-gap length. As previously described in the Air section of motor materials, 3.1.2, the air-gap is a crucial part for the motor reliability and provides significant effects on the performance. With the increase of the motor poles, those effects rise considering that the magnetic flux crosses the air-gap more times for each rotor revolution.

Since it takes more current to drive flux through the air than through steel, a smaller gap is desirable, as it reduces the magnetising current. On one hand, the longer thickness between the motor and the stator results in high eddy current loss, weaker Lorentz force and lower values of torque and motor's efficiency, however, on the other hand, core losses increase with the decrease of the air-gap length.

For the model design optimisation, the air-gap length, opposed from prediction, was not reduced to its minimum value. This distance was defined with a minimum value of 1 mm due to mechanical problems alongside with noise and losses, as described in the previously mentioned Air section of motor materials, 3.1.2.

Regarding this, the electromagnetic performance of the air-gap in the model was studied and discussed. Being presented in Fig. 5.13 and Fig. 5.14.

The optimised machine used for the study was the one nearest to the 20 Nm value for the FeSi material, shown in Fig.5.13(a) , where the NSGA-II algorithm optimised the air-gap length to 1.4 mm. Using this machine and it's optimised values presented in tables 5.3 and 5.4, a FEM simulation was done with the air-gap length chosen to a fixed value of 1 mm.

The machine resulting from this simulation can be observed in Fig. 5.13(b) and analysing its values in tables 5.3 and 5.4, its noticeable that the value of the maximum magnetic flux overcomes the magnetic constraint of 1.6 T. Being this the reason why the optimised machine has 1.4 mm of air-gap length instead of the minimum value of 1 mm.

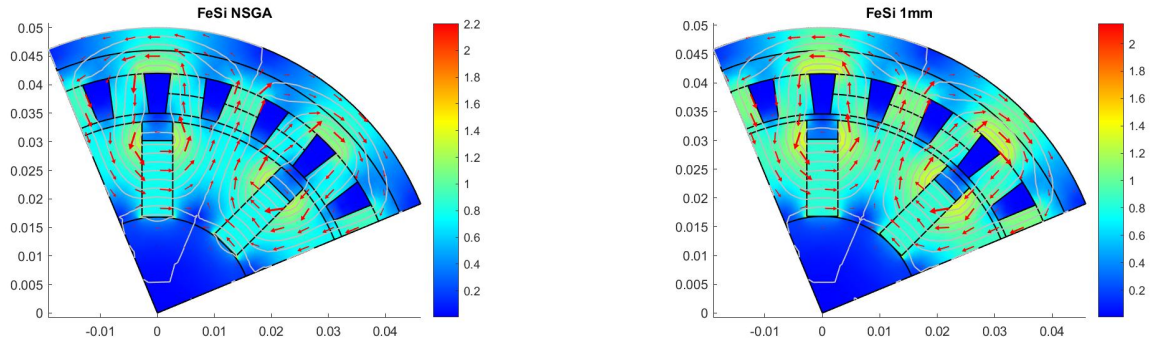

(a) NSGA-II optimisation

(b) Air-gap length equal to 1mm

Figure 5.13: Air-gap study for the FeSi material.

The same study was done for the equivalent machine for the VCoFe material. An optimised machine with the nearest efficiency value of the one studied for the FeSi material was chosen and is presented in Fig. 5.14(a).

FeSi	T [Nm]	η	B_{max} [T]	Ψ_{PMd} [Wb]	I_{max} [A]	Jm_{th} [A/m^2]	P_{cu} [W]	P_{core} [W]	Vol [m^3]
NSGA (1.4mm)	**19.5170**	**0.9530**	1.4988	0.0048	673.4589	5.3095e7	536.3415	68.1544	4.2439e-4
1 mm	22.1835	0.9571	**1.6879**	0.0056	654.7980	5.3289e7	521.3189	103.0798	4.2278e-4

Table 5.3: Optimisation results for the FeSi material.

FeSi	Jm [MA/m^2]	r_r [mm]	r_s [mm]	w_m [mm]	l_m [mm]	w_t [mm]	l_t [mm]	w_s [mm]
NSGA	25.4568	336	168	54	134	63	70	1.4

Table 5.4: Optimisation dimensions for the FeSi material.

Once again, an FEM simulation with the air-gap length value of 1 mm was done, Fig. 5.14(b). Observing the results of this simulation in tables 5.5 and 5.6, it can be detected that one more time the maximum value of magnetic flux density, 2.2 T for VCoFe, was exceeded. And for this reason, the optimised model set the air-gap length to 1.3 mm instead of the minimum value of 1 mm.

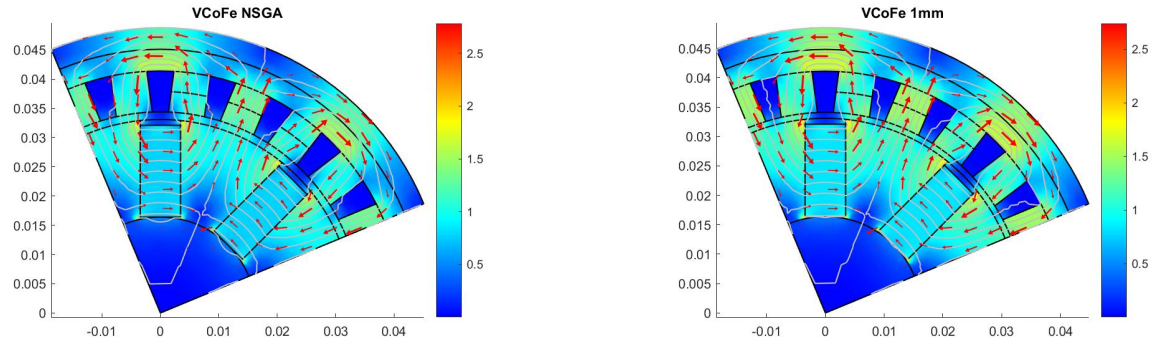

(a) NSGA-II optimisation

(b) Air-gap length equal to 1mm

Figure 5.14: Air-gap study for the VCoFe material.

VCoFe	T [Nm]	η	B_{max} [T]	Ψ_{PMd} [Wb]	I_{max} [A]	Jm_{th} [A/m^2]	P_{cu} [W]	P_{core} [W]	Vol [m^3]
NSGA (1.3mm)	34.5427	**0.9534**	2.0085	0.0064	897.1595	5.2570e7	960.9458	110.1128	3.8510e-4
1 mm	37.5871	0.9563	**2.2620**	0.0071	878.2291	5.2536e7	940.2291	140.0961	3.8398e-4

Table 5.5: Optimisation results for the VCoFe material.

VCoFe	Jm [MA/m^2]	r_r [mm]	r_s [mm]	w_m [mm]	l_m [mm]	w_t [mm]	l_t [mm]	w_s [mm]
NSGA	34.4328	331	164	69	157	62	70	1.3

Table 5.6: Optimisation dimensions for the VCoFe material.

Chapter 6

Conclusions

An overall consideration about the work carried out, alongside with the achievements and results of the entire project, is hereby conducted.

In the future work section, several methods and new approaches to improve the EMs optimisation and global performance, as well as defining the viability and the benefits of using VCoFe as core magnetic material, are suggested for the future studies regarding this topic.

Contents

6.1 Achievements

The main objective of this project was to define where using VCoFe alloy, holding a remarkable high saturation point of 2.2-2.4 T, provides an advantageous utilisation in a high specific-power spoke-type IPMSM for the worldwide competition's FST electric car, demanding high-performance requirements with a large ratio of power/volume. The typical FeSi and the newly used VCoFe metallic alloys have been considered as the magnetic core material of the EM, to provide a general comparative analysis between the two of them.

The main literature on the use of PMSM in an electric racing car and other specific traction application, along with the different possible materials used in the manufacturing of an EM is reviewed. The manufacturing and post-processing various procedures and techniques were analysed and how it affects the final magnetic properties. Different magnetic circuits geometries were designed and studied to meet the FST performance specifications and defined requirements.

Due to the multiphysics complexity (electromagnetic, mechanical and thermal, with non-linear materials) and to high number of variables and constraints, a multi-objective optimisation was applied with NSGA-II algorithm coupled with a hybrid analytical/FEM to provide sufficiently accurate electromagnetic and thermal results within a feasible time. This approach allowed to identify the best parameters and machine designs, using VCoFe and FeSi, regarding the two objective functions of maximising torque production and efficiency, while fulfilling the relevant applicable constraints. A visualisation of the Pareto front and the analysis of the different variables along the optimised solutions is additionally possible with the use of this optimisation's algorithm.

Each genetic optimisation was done for 150 generations with 200 population elements each, meaning that 30000 different motor geometries were tested, which was enough for the solution to converge within a feasible time of 26 hours for FeSi and 30 hours for VCoFe, due to the low computational time of the developed electromagnetic and thermal model.

The developed hybrid model is composed of a stationary time 2D FEM, to calculate the motors main parameters such as $d-q$ inductances and magnetic flux distribution, and an auxiliary analytical script to compute voltage, losses, electromagnetic torque and efficiency. The electromagnetic and thermal model's investigation was conducted applying each material's B-H magnetisation curve and losses, to increase the motor's reliability and performance, where the opted cooling system to apply was previously developed in a preceding study.

Results from the Pareto front demonstrate VCoFe as a beneficial core material choice across both torque and efficiency ranges, while providing higher power densities than FeSi. Outperforming FeSi in an estimated increase of up to 3% in efficiency for the same torque, or up to 70% torque increase for the same efficiency level. For the competition car, with a required 20 Nm of nominal torque, there is an efficiency increase of 1.7% and a reduction of 11% in the magnetic core volume for the motor. Enabling the motor optimised with VCoFe to reach up to 40 Nm where, for the same available space and with similar levels of efficiency, FeSi only reaches 24 Nm. However, due to the higher material density of VCoFe, a more tenuous variation in core weight is observed, compared to FeSi.

Analysing each of the decision variables, it is possible to determine that the performance of the motor is limited by the saturation curve of the ferromagnetic material, however, due to the cooling system applied, it has high thermal safety margin.

Therefore, it can be concluded that using VCoFe alloy as a core material has a high impact on the efficiency and global performance of the motor. Appearing to be a great option for the core material of traction motor applications where the volume and performance overcome the importance of the final price, as in aeronautical and, as the FST, racing environment.

6.2 Future Work

The project results and achievements demonstrate the possibility of building a competitive tailored motor in the future. Designing a geometry adaptable and fully customisable to the requirements of a racing car like the FST, instead of adapting commercial solutions which are more expensive and more ordinary.

In what concerns the future studying for the motor's improvement, it is proposed to proceed to the design of the model with different configurations as number of poles, number of slots, number of turns per coil and any target specifications.

Another approach would result in the use of multiple materials for different parts of the EM's core, i.e. using VCoFe in the rotor, where losses are lower, providing a higher magnetic flux density, and using FeSi or SMC in the stator, to reduce the core losses impact on performance although lowering the volume density.

A 3D FEM time-dependent model must be developed allowing a more complete simulation to study the border effects, harmonics, noise and torque ripple. With the core losses being computed using the hysteresis Jiles-Atherton model and the thermal model considering all materials and cooling fluid.

Furthermore, building a test-bench to fully test the performance of the designed and optimised motor should be achieved. Prototyping and testing to evaluate the machine's performance maps, in terms of developed torque, efficiency, power factor and operation constraints. Allowing the validation, and re-calibration, of both 2D and 3D IPMSM FEMs.

Due to the post-processing required to achieve optimal properties of VCoFe laminations and to the cobalt's value, the prices arise. To establish whether the additional costs of manufacturing VCoFe laminations compared with FeSi are justified or not, regarding the difference in specific torque and the increase in efficiency, has to be subject to further application-specific cost/benefit analysis. This analysis is also carried to take into account the impact of using this material on battery size and overall track performance.

Bibliography

[1] T. V. Jayaraman, “Effect of Processing of HIPERCO® 50 Alloy Laminates on Their Magnetic Properties,” *Journal of Electronic Materials*, vol. 44, no. 11, pp. 4379–4386, 2015.

[2] B. A. Krings, M. Cossale, A. Tenconi, J. Soulard, A. Cavagnino, and A. Boglietti, “Magnetic Materials Used in Electrical Machines,” *IEEE Industry Applications Magazine*, vol. 23, no. 6, pp. 21–28, 2017.

[3] A. Krings, A. Boglietti, A. Cavagnino, and S. Sprague, “Soft Magnetic Material Status and Trends in Electric Machines,” *IEEE Transactions on Industrial Electronics*, vol. 64, no. 3, pp. 2405–2414, 2017.

[4] X. Zhang and K. S. Haran, “High-specific-power electric machines for electrified transportation applications-technology options,” *ECCE 2016 - IEEE Energy Conversion Congress and Exposition, Proceedings*, 2016.

[5] M. Palmieri, M. Perta, and F. Cupertino, “Design of a 50.000-r/min synchronous reluctance machine for an aeronautic diesel engine compressor,” *IEEE Transactions on Industry Applications*, vol. 52, no. 5, pp. 3831–3838, 2016.

[6] N. Fernando, G. Vakil, P. Arumugam, E. Amankwah, C. Gerada, and S. Bozhko, “Impact of Soft Magnetic Material on Design of High-Speed Permanent-Magnet Machines,” *IEEE Transactions on Industrial Electronics*, vol. 64, no. 3, pp. 2415–2423, 2017.

[7] B. C. Mecrow, A. G. Jack, D. J. Atkinson, S. R. Green, G. J. Atkinson, A. King, and B. Green, “Design and testing of a four-phase fault-tolerant permanent-magnet machine for an engine fuel pump,” *IEEE Transactions on Energy Conversion*, vol. 19, no. 4, pp. 671–678, 2004.

[8] N. Volbers and J. Gerster, “High Saturation , High Strength Iron-Cobalt Alloy for Electrical Machines,” *Proceedings of the INDUCTICA, CWIEME*, pp. 1–4, 2012.

[9] P. P. C. Bhagubai, J. G. Sarrico, J. F. P. Fernandes, and P. J. C. Branco, “Multi-Objective Optimization, and Prototyping of a 20 kW 8000 rpm Permanent Magnet Synchronous Motor for a Competition Electric Vehicle,” *Energies*, vol. 13, no. 10, p. 2465, 2020.

[10] B. K. Lee, G. H. Kang, J. Hur, and D. W. You, “Design of spoke type BLDC motors with high power density for traction applications,” *Conference Record - IAS Annual Meeting (IEEE Industry Applications Society)*, vol. 2, pp. 1068–1074, 2004.

[11] K. Deb, A. Pratap, S. Agarwal, and T. Meyarivan, “A fast and elitist multiobjective genetic algorithm: NSGA-II,” *IEEE Transactions on Evolutionary Computation*, vol. 6, no. 2, pp. 182–197, 2002.

[12] Z. Yang, F. Shang, I. P. Brown, and M. Krishnamurthy, “Comparative study of interior permanent magnet, induction, and switched reluctance motor drives for EV and HEV applications,” *IEEE Transactions on Transportation Electrification*, vol. 1, no. 3, pp. 245–254, 2015.

[13] G. Abad, *Power Electronics and Electric Drives for Traction Applications*. John Wiley & Sons, Ltd., 2016.

[14] G. Pellegrino, A. Vagati, B. Boazzo, and P. Guglielmi, “Comparison of induction and PM synchronous motor drives for EV application including design examples,” *IEEE Transactions on Industry Applications*, vol. 48, no. 6, pp. 2322–2332, 2012.

[15] B. Ricardo da Fonseca Marques, “Virtual Prototyping of a Brushless Permanent Magnet AC Motor - Electromagnetic and Thermal Design using CAD Software,” no. November, p. 134, 2012.

[16] “Technological feasibility studies for super and ultra premium efficient motors,” Conseil international des grands réseaux électriques. Comité d’études A1, CIGRÉ, 2018.

[17] G. E. Fish, “Soft Magnetic Materials,” *Proceedings of the IEEE*, vol. 78, no. 6, pp. 947–972, 1990.

[18] H. Gavrila and V. Ionita, “Crystalline and amorphous soft magnetic materials and their applications - Status of art and challenges,” *Journal of Optoelectronics and Advanced Materials*, vol. 4, no. 2, pp. 173–192, 2002.

[19] V. Ionita, E. Cazacu, and L. Petrescu, “Effect of voltage harmonics on iron losses in magnetic cores with hysteresis,” *Proceedings of International Conference on Harmonics and Quality of Power, ICHQP*, vol. 2018-May, no. 2, pp. 1–5, 2018.

[20] R. S. Sundar and S. C. Deevi, “Soft magnetic FeCo alloys: Alloy development, processing, and properties,” *International Materials Reviews*, vol. 50, no. 3, pp. 157–192, 2005.

[21] M. Centner and U. Schäfer, “Optimized design of high-speed induction motors in respect of the electrical steel grade,” *IEEE Transactions on Industrial Electronics*, vol. 57, no. 1, pp. 288–295, 2010.

[22] E. W. Fairall, B. Bilgin, and A. Emadi, “State-of-the-art high-speed switched reluctance machines,” *Proceedings - 2015 IEEE International Electric Machines and Drives Conference, IEMDC 2015*, pp. 1621–1627, 2016.

[23] W. U. Fernando and M. Barnes, “Electromagnetic energy conversion efficiency enhancement of switched reluctance motors with zero-voltage loop current commutation,” *IEEE Transactions on Energy Conversion*, vol. 28, no. 3, pp. 482–492, 2013.

[24] M. Palmieri, M. Perta, F. Cupertino, and G. Pellegrino, “High-speed scalability of synchronous reluctance machines considering different lamination materials,” *IECON Proceedings (Industrial Electronics Conference)*, pp. 614–620, 2014.

[25] P. P. Bhagubai and J. F. Fernandes, “Multi-objective optimization of electrical machine magnetic core using a vanadium-cobalt-iron alloy,” *IEEE Transactions on Magnetics*, vol. 56, no. 2, 2020.

[26] A. C. Smith and D. Delgado, “Automated AC winding design,” *IET Conference Publications*, vol. 2010, no. 563 CP, 2010.

[27] J. B. Gonçalo Viseu Vieira Sarrico, *Design and Implementation of a 20 kW, 12000 RPM Permanent Magnet Synchronous Motor (PMSM) for the IST Formula Student Powertrain Electrical and Computer Engineering Examination Committee*. PhD thesis, Técnico Lisboa, 2017.

[28] C. L. Torres, “Analysis and implementation of a methodology for optimal PMa-SynRM design taking into account performances and reliability,” 2018.

[29] J. Y. Lee, S. H. Lee, G. H. Lee, J. P. Hong, and J. Hur, “Determination of parameters considering magnetic nonlinearity in an interior permanent magnet synchronous motor,” *IEEE Transactions on Magnetics*, vol. 42, no. 4, pp. 1303–1306, 2006.

[30] K. Yamazaki, T. Fukuoka, K. Akatsu, N. Nakao, and A. Ruderman, “Investigation of locked rotor test for estimation of magnet PWM carrier eddy current loss in synchronous machines,” *IEEE Transactions on Magnetics*, vol. 48, no. 11, pp. 3327–3330, 2012.

[31] S. H. Han, T. M. Jahns, and Z. Q. Zhu, “Analysis of rotor core eddy-current losses in interior permanent-magnet synchronous machines,” *IEEE Transactions on Industry Applications*, vol. 46, no. 1, pp. 196–205, 2010.

[32] W. Y. Huang, A. Bettayeb, R. Kaczmarek, and J. C. Vannier, “Optimization of magnet segmentation for reduction of eddy-current losses in permanent magnet synchronous machine,” *IEEE Transactions on Energy Conversion*, vol. 25, no. 2, pp. 381–387, 2010.

[33] P. M. d. A. Fontes, *Refrigeração do propulsor elétrico de um veículo Formula Student*. PhD thesis, Técnico Lisboa, 2016.

[34] M. Popescu, D. Staton, A. Boglietti, A. Cavagnino, D. Hawkins, and J. Goss, “Modern heat extraction systems for electrical machines - A review,” *Proceedings - 2015 IEEE Workshop on Electrical Machines Design, Control and Diagnosis, WEMDCD 2015*, pp. 289–296, 2015.

[35] W. Shi, J. Liu, and C. Li, “Effect of cutting techniques on the structure and magnetic properties of a high-grade non-oriented electrical steel,” *Journal Wuhan University of Technology, Materials Science Edition*, vol. 29, no. 6, pp. 1246–1251, 2014.

[36] A. Ali and M. Yeakub, “Application of Silicon Carbide in Abrasive Water Jet Machining,” *Silicon Carbide - Materials, Processing and Applications in Electronic Devices*, no. August 2014, 2011.

[37] A. Schoppa, H. Louis, F. Pude, and C. Von Rad, “Influence of abrasive waterjet cutting on the magnetic properties of non-oriented electrical steels,” *Journal of Magnetism and Magnetic Materials*, vol. 254-255, pp. 370–372, 2003.

[38] A. Belhadj, P. Baudouin, F. Breaban, A. Deffontaine, M. Dewulf, and Y. Houbaert, “Effect of laser cutting on microstructure and on magnetic properties of grain non-oriented electrical steels,” *Journal of Magnetism and Magnetic Materials*, vol. 256, no. 1-3, pp. 20–31, 2003.

[39] K. Gupta and N. Jain, “Manufacturing of High Quality Miniature Gears by Wire Electric Discharge Machining,” in *DAAAM INTERNATIONAL SCIENTIFIC BOOK 2013*, ch. 40, pp. 679–696, Vienna, Austria: DAAAM International, 2013.

[40] A. Boglietti, A. Cavagnino, L. Ferraris, and M. Lazzari, “The annealing influence onto the magnetic and energetic properties in soft magnetic material after punching process,” *IEMDC 2003 - IEEE International Electric Machines and Drives Conference*, vol. 1, pp. 503–508, 2003.

[41] A. Krings, S. Nategh, O. Wallmark, and J. Soulard, “Influence of the welding process on the magnetic properties of a slot-less permanent magnet synchronous machine stator core,” *Proceedings - 2012 20th International Conference on Electrical Machines, ICEM 2012*, vol. 2, no. 1, pp. 1333–1338, 2012.

[42] Wei Tong, *Mechanical Design of Electric Motors*, vol. 6. CRC Pres, Taylor & Francis Group, 1985.

Appendix A

Treatment of Laminated Material

A.1 Cutting Process

The cutting process involving the non-oriented electrical sheets has an impact on the electromagnetic properties of the alloys. The chosen process can cause stress and deterioration on the electrical steel, thus affecting its magnetic properties and increasing the iron losses. These effects can be observed in Fig. A.1.

The most common cutting technologies are stamping process, water-jet cutting, laser cutting and Wire-Electrical Discharge Machining WEDM.

Additional techniques include guillotine shear, photo-corrosion or electron beam machining.

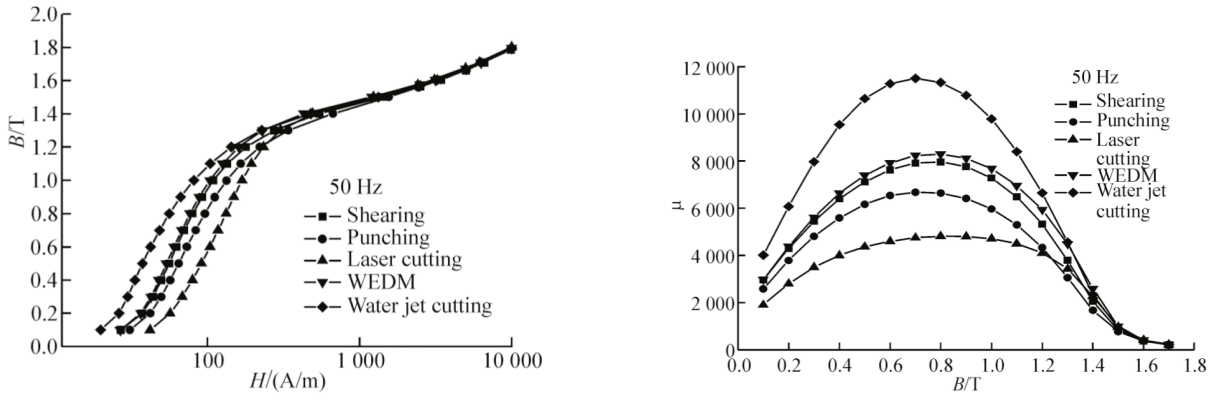

(a) B-H curve of cutting techniques

(b) μ-B curve of cutting techniques

Figure A.1: The effects of cutting techniques on both the B-H and the μ-B curves [35].

A.1.1 Stamping Process

Stamping, or pressing process, involves using a press to stamp a die, with the desired design, against flat sheet metal. Punching, blanking, bending, coining, embossing, and flanging are all stamping techniques used to shape the metal. It could be a single stage operation where every stroke of the press produces the desired form on the sheet metal part or could occur through a series of stages.

This procedure stresses the material and changes its compound, leading to unfavourable changes in the iron losses and the material's saturation point. As a consequence of this, an annealing process is made before or after the stamping process to regenerate the magnetic properties of the material [1].

It is the most common process to achieve electrical engine core and the cheapest one as well. Is usually done on cold metal sheets.

A microscopic analysis of the cut section using stamping technique can be see in figures A.7(a), A.7(b), and A.7(c).

A.1.2 Water-Jet Cutting

Water-jet cutting uses an industrial tool capable of cutting a wide variety of materials using a very high-pressure jet of water, or a mixture of water and an abrasive substance. This cutting technology is shown in Fig. A.2.

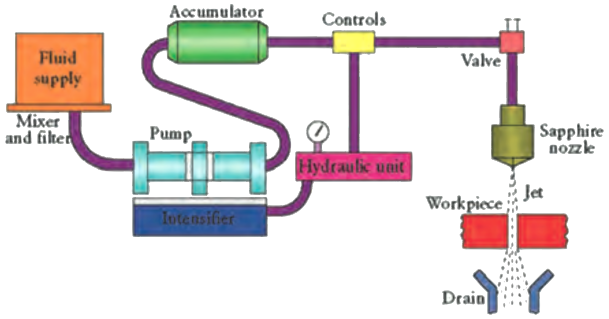

Figure A.2: Working principle of water-jet cutting [36].

The advantages of this technology are not creating thermal stresses or plastic deformation, being the preferred method for materials which are sensitive to high temperatures, offering the lowest total material losses in the cutting area and absence of the need for annealing treatment which would increase the final cost. However, this technique delivers less precision on the cut and creates small mechanical deformations [37].

Water-jet cutting is used in various industries, including mining and aerospace, for cutting, shaping, and reaming.

A.1.3 Laser Cutting

Laser cutting is a technology that uses a high-power laser beam to cut through the materials, causing a thermal effect in the area of the cut, which either melts, burns, vaporises away or is blown by a jet of gas.

Because of the non-contact cutting effect, it avoids the shearing deformation and the generation of a burr at the cutting edges, leaving the edges with a high-quality surface finish and increasing the flexibility. Concluding that it causes the reduction of the undesirable cutting effects on magnetic properties and, cooperating with an annealing process, it increases the magnetic properties of the material [35].

There are some drawbacks on choosing this method. Laser cutting causes a coercive field increase and permeability drop, due to the thermal effects of material heating until the molten partially evaporated stage, that leads to internal stress and modifications on the material microstructure [38].

Even though it allows manufacturers to easily design motors, laser cutting is more time consuming and expensive way to go.

A.1.4 Wire-Electrical Discharge Machining (WEDM)

WEDM is a process of metal machining where an electro-thermal wire, usually copper or tin, cuts electrically conductive materials discharging thousands of sparks to the metal piece while both are immersed in deionised water. WEDM is not one of the most common cutting processes, yet it works on parts resistant to conventional cutting processes if these parts are electrically conductive. The material removal mechanism consists in flushing away the material by the flowing dielectric fluid, since the area where discharge takes place is heated to an extremely high temperature that leads to melting, instead of the typical cut, leaving little debris and providing a very accurate line. A voltage is applied between the lamination and the wire, creating a channel of plasma in the working gap and the discharge takes place with a heavy flow of current within it. This working principle can be observed in Fig. A.3

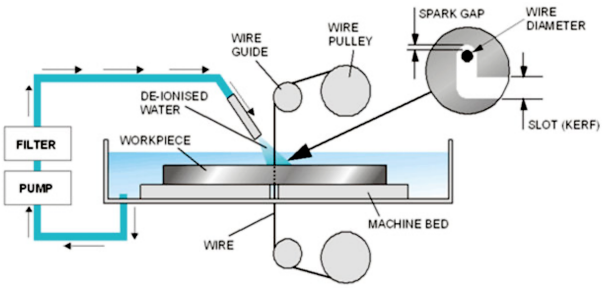

Figure A.3: Working principle of WEDM [39].

The major benefits of electing this technology are that the mechanical stress machining is eliminated, given that there is no contact between the wire and the steel piece. Consequently, the residual stress created by WEDM is mostly thermal and the residual one can be negligible, usually eliminating the need for a pos-annealing process and reducing costs and manufacturing time [1].

Industry-wide acceptance has led to a wide variety of WEDM applications in various industries such as aerospace, automotive, and renewable energy for cutting complex, intricate, precise and irregular shapes being highly versatile and requiring a relatively compact amount of work-space.

A microscopic analysis of the cut section using WEDM technology can be see in figures A.7(d), A.7(e), and A.7(f).

A.2 Annealing Process

The chosen cutting process, most often, deteriorates the materials during manufacturing and changes the magnetic properties of these. A thermal treatment concerning a specialised coating process called

annealing can, to a great extent, restore this deterioration enhancing the magnetic properties and the mechanical characteristics of the finished laminations. The choice of whether to anneal a material or not is mainly a question of costs since newly developed grades of FeSi, amorphous materials and SMC materials can be delivered in a fully-processed condition, offering the elimination of the standard post-cutting annealing and oxide coating processes and keeping the costs low. Despite that, for materials such as NiFe and VCoFe the annealing process, to obtain the desired magnetic properties is essential [40].

The mechanical strength of the material and its magnetic permeability can be controlled by changing the temperature cycle during the annealing process, where it typically ranges between 750 to 950° C. However, the magnetisation of ferromagnetic materials is heavily dependent on the magnetic domains, which are related to the grain structure of the ferromagnetic material, so, a trade-off must be made between the magnetic and mechanical properties. Higher annealing temperatures leads to grain size growth implying better magnetic properties and higher saturation magnetisation, whereas lower annealing temperatures are favourable to improve the mechanical strength and hardness of the material. Small grains cause a high coercivity and larger grains a lower coercivity. This linear relationship between annealing temperature and yield strength is illustrated in Fig. A.4. Therefore, the annealing process should be adapted to the needs of the machine design requirements [3].

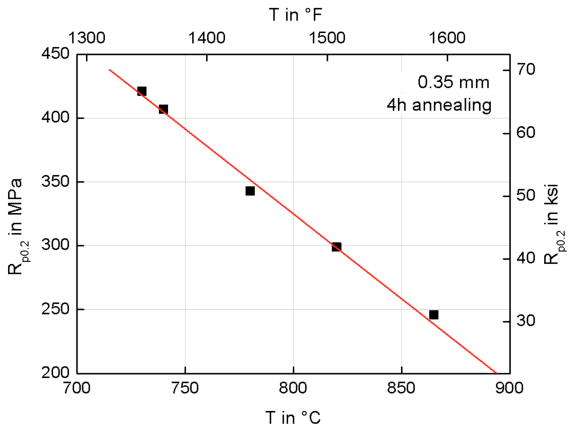

Figure A.4: Dependence of the yield strength from the annealing temperature [8].

Additionally to the time and temperature of annealing, the sequence between cutting and annealing is as well an important aspect of the manufacturing of the final product. Fig. A.5 exhibits the B-H curves of the VCoFe sheets for the different sequences of annealing combined with stamping and WEDM cutting processes showed in Fig. A.7. Significantly superior soft-magnetic characteristics are noticeable in the annealed material. The sequence of the cutting process is more significant in the stamping method, where the annealing followed by stamping has distinct magnetic properties compared to stamping followed by annealing. In contrast, the WEDM cutting technology has light changes regarding the sequence of annealing. It is also noticeable that the characteristics of the material are almost re-established after annealing and the best magnetic properties can be achieved.

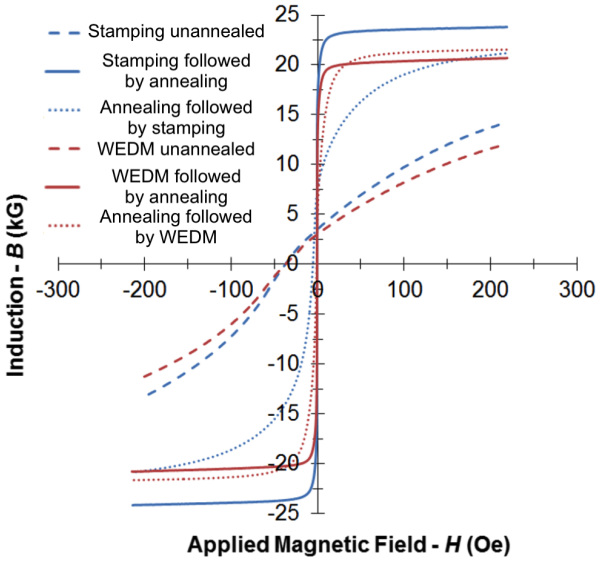

Figure A.5: B-H curves of the VCoFe sheets annealing, stamping and WEDM processes combinations [1].

A microscopic analysis is used to study the grain structure of the materials before and after the annealing process in [2] and [1].

In Fig. A.6 a microscopic study of the VCoFe sheets grain structure is presented and it can be observed how different annealing methods modify the micro-graphic structure. While in Fig. A.6(a), where the sample is not annealed, a structure is not recognisable, in Fig. A.6(b) and Fig. A.6(c), where it is annealed for two hours at 760° C and three hours at 850° C respectively, the structure is well recognised with grain sizes reaching up to 20 and 100 μm.

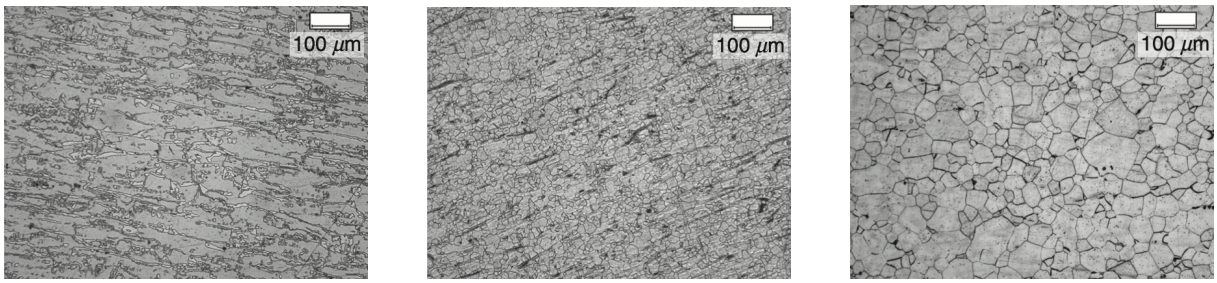

(a) No annealing (b) 2 hours of 760° C annealing (c) 3 hours of 850° C annealing

Figure A.6: Microscopic study of the VCoFe sheets annealing methods on the grain structure [2].

Multiple sequences can be observed in Fig. A.7 for stamping and WEDM cutting processes. With the stamping, a trimmed surface is left by the cutting process, as seen in figures A.7(a), A.7(b), and A.7(c), where the sequence of the annealing process brings changes to the smoothness of the material's surface. In figures A.7(d), A.7(e), and A.7(f), where the cutting technology used is the WEDM, a rough surface is observed even though the annealing process smoothes it.

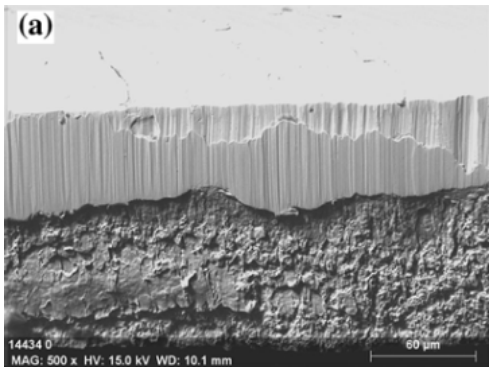

(a) Stamping unannealed

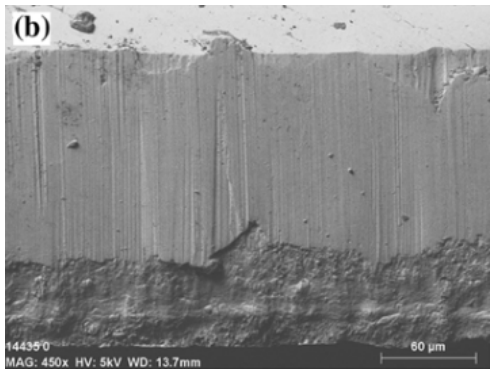

(b) Stamping followed by annealing

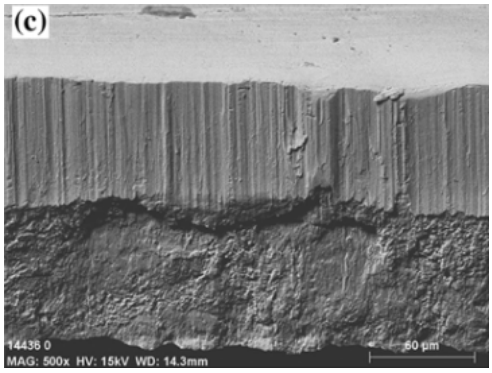

(c) Annealing followed by stamping

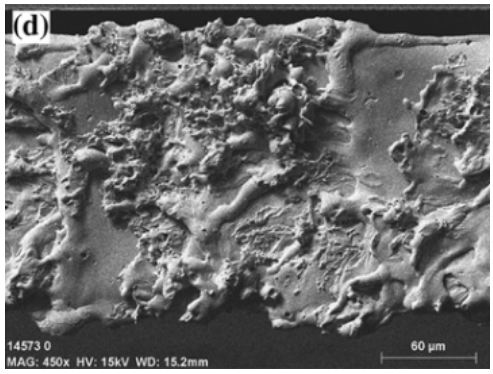

(d) WEDM unannealed

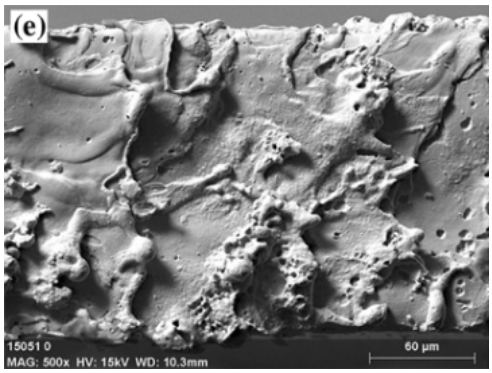

(e) WEDM followed by annealing

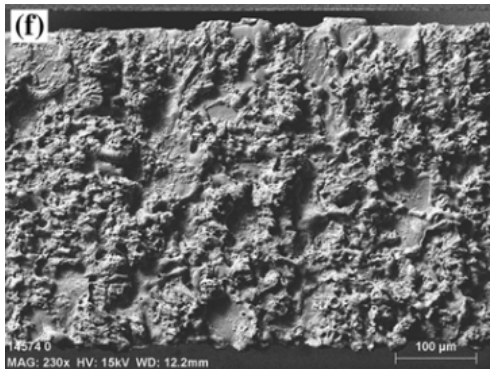

(f) Annealing followed by WEDM

Figure A.7: Microscopic study of the VCoFe sheets annealing, stamping and WEDM processes combinations [1].

In [8], the use of annealing also made feasible to stamp the stator and rotor lamination from the same material adjusting their heat treatment. Making possible to yield strength requirements, both on rotor and stator, to be met for optimum properties. Resulting in less material consumption, robust heat treatment process and more flexible material regarding the mechanical properties.

This study makes it obvious that the annealing process is indispensable for obtaining the full magnetic performance of VCoFe lamination sheets. Leading to a reduction of iron losses in the EMs overall performance. Where stamping followed by annealing appears to be the best approach to the manufacturing process.

A.3 Stacking Process

The stacking process consists of stacking all the steel laminations together for the rotors and stator's core manufacturing. Several technologies of stacking are available in the market, and since these have different influences, on the overall motor efficiency, iron losses and mechanical structure, it is mandatory to choose the right method for the desired application.

A.3.1 Welding

Welding is the most ordinary method and it involves joining the metal sheets together by using high heat to melt the parts together and allowing them to cool, causing fusion. To ease this process normally is made a slot on the stator without increasing the stator diameter. A filler material is commonly added to the joint to form a pool of molten material that cools to form a joint, visualised in Fig. A.8.

This technology promotes contact with the different sheets, decreasing their resistance and increasing the eddy currents.

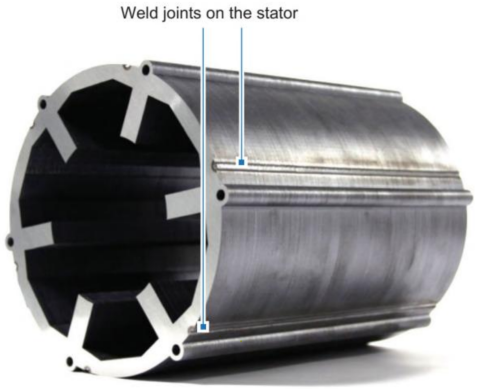

Figure A.8: Welding technique used around the stator core [41].

A.3.2 Riveting

Riveting is the process of holding all the metal sheets together with a permanent mechanical fastening. It has low costs since it is simple to do and is capable of supporting tension loads, once there is effectively a head on each end of an installed rivet. Considering that rivets obstruct the stator windings, the use of pins is also feasible.

A.3.3 Thin Sleeves

This method consists in the use of thin metallic sleeves to secure the stator core at the outside of the core, as can be seen in Fig. A.9, relying on the shrink fit technique. It is opted in machines that need to withstand large forces with only tiny deformation, as the sleeves, normally made from metal, have high strength. Losses due to induced currents are a common drawback of this technology as they highly influence the machine overall efficiency.

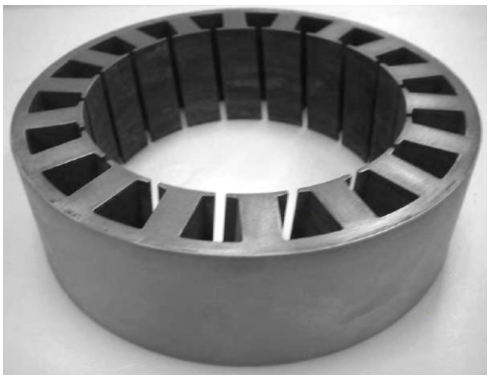

Figure A.9: Stator core with a thin sleeve at the outside of the core [42].

A.3.4 Adhesive Bonding

Bonding with adhesive materials is the procedure to join two surfaces together, with the creation of a smooth bond. Through chemical and physical curing, the adhesive changes from a liquid or pasty state to a solid-state. In the liquid state, the good wetting properties enable the adhesive to get close enough to the substrate in such a way that molecular interaction between substrates and adhesive is enabled. After the curing reaction, cohesion or internal strength is built up.

Eventually, the electric steel sheets can be ordered already with a thin film adhesive already placed. Even though this technology provides low mechanical strength of the stack it improves efficiency and does not increase eddy currents losses.

A.3.5 Cleating

Cleating consists in process ”V” shaped strips of soft steel and then flatten them down a dovetail slot at the outer diameter face of the stator or rotor laminations. As seen in Fig. A.10. This method is of fast manufacturing, requires little set-up and has low costs. Cleating still leaves the stator with good electrical properties and the cleats are easily stripped out to salvage rejected cores. The disadvantage is the simplicity of the process getting lower with the decrease of the motor’s volume.

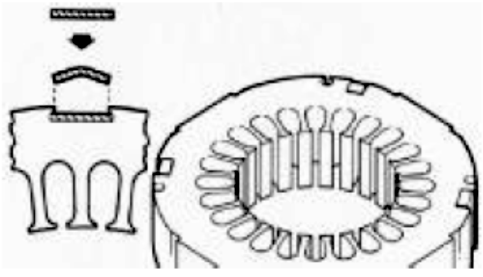

Figure A.10: Cleating method schematic [42].